Title: HSD17B7 is required for Auditory Function by Regulating Cholesterol Synthesis in Sensory Hair Cells

Running title: HSD17B7 Regulates Auditory Function

Yuqian Shen [1, *], Ziyang Wang [1, *], Xun Wang [1], Fuping Qian [2], Mingjun Zhong [3], Xin Wang [2, #], Jing Cheng [3, #], Dong Liu [1, #]

[1] Nantong Laboratory of Development and Diseases, School of Life Sciences, Co-innovation Center of Neuroregeneration, Nantong University, Nantong 226001, China.

[2] Institute of Special Environmental Medicine, Nantong University, Nantong 226001, China.

[3] Institute of Rare Diseases, West China Hospital of Sichuan University, Chengdu, 610044 China.

* These authors contributed equally to this work

#, author for correspondence

Contact details for Correspondence:

Dong Liu, Ph.D.

Nantong Laboratory of Development and Diseases, Nantong University

Qixiu Road 19, Nantong, China, 226001

Phone: + (86) - 18605133927

Email: liudongtom@gmail.com; tom@ntu.edu.cn

Abstract

An imbalanced cholesterol level is a root cause of various pathologies. However, research on the role of cholesterol homeostasis in hearing physiopathology is still in its infancy. HSD17B7 (17β-Hydroxysteroid dehydrogenase type 7) converts zymosterone to zymosterol in the process of cholesterol synthesis. Here, we found that Hsd17b7 is highly enriched in sensory hair cells of zebrafish and mice. The deficiency of Hsd17b7 led to reduced cholesterol levels in HEI-OC1 cells and hair cells of zebrafish, resulting in compromised MET and auditory function. A heterozygous nonsense variant, c.544G>T (p.E182*) in *HSD17B7* was identified in an individual with bilateral profound hearing loss. mRNA of HSD17B7(p. E182*) failed to rescue the impaired MET and auditory function of hsd17b7 mutants. The mutation of HSD17B7 disrupted its interaction with RER1, leading to altered localization and cholesterol distribution. This provides an explanation for the pathogenic effect of the heterozygous mutation observed in the human case and zebrafish. The current study highlights HSD17B7 as a novel gene linked to sensorineural hearing loss.

Keywords

HSD17B7; cholesterol ; hair cell; hearing loss

Introduction

Deafness is a common and highly disabling disease in humans that has not been effectively prevented or controlled. According to a survey report by the World Health Organization, the number of people suffering from deafness worldwide reached 466 million, accounting for more than 5% of the global population. By 2050, nearly 2.5 billion people are projected to have some degree of hearing loss. Deafness has become a major concern for global health. According to the 2016 population survey in China, approximately 70 million people experienced hearing loss. Among children in Jilin, Gansu, Guangdong, and Shanxi provinces of China, the prevalence rate of disabling hearing loss is 0.85%, and it is expected that this prevalence rate will increase year by year [1]. According to pathogenic factors, about 60% of deafness is caused by a genetic defect known as hereditary deafness. Investigating the genetic identification and molecular mechanisms of hereditary deafness would reveal the occurrence and development of the disease, which is the cornerstone of accurate diagnosis and prevention of deafness. Geneticists estimate that the total number of genes responsible for deafness is more than 1000. So far, around 156 non-syndromic deafness genes have been identified [2], and there are still a large number of new deafness genes that need to be identified.

Cholesterol is the most abundant sterol molecule in mammalian cells. It constitutes the cell membrane and is crucial in synthesizing important hormones, facilitating synapse formation, and mediating cell signaling transduction [3-6]. Previous studies have shown that dysregulated intracellular cholesterol homeostasis in auditory cells is involved in auditory development defects [6-8], hereditary hearing loss [9-13], noise-induced hearing loss [14-16], ototoxic hearing loss [17, 18], and age-related hearing loss [19-21]. It has been demonstrated that HSD17B7 converts zymosterone to zymosterol during the cholesterol synthesis process, and is expressed in the brain, heart, eye, and ear [22, 23]. However, the function of HSD17B7 in the auditory system remains unexplored. No pathogenic HSD17B7 mutations have been reported to be associated with hearing loss. Here, we show that HSD17B7 is highly expressed in sensory hair cells in mice and zebrafish. Our findings highlight the critical role of HSD17B7 in the auditory system, positioning it as a potential therapeutic target for hearing loss.

Results

Hsd17b7 expressed in sensory hair cells of zebrafish and mice

To assess the role of *HSD17B7* in the auditory system, we first investigated the expression of the *hsd17b7* in the developing zebrafish. Single-cell data analysis (accession no. GSE221471) [24] categorized neuromast hair cell (cluster 0), supporting cell (cluster 1), macula hair cell (cluster 2), crista hair cell 1 (cluster 3), mantle cell (cluster 4) and crista hair cell 2 (cluster 5) using the Seurat 4.0.1 platform (Figure 1A). The feature plot and violin plot showed that *hsd17b7* was expressed in sensory hair cells, especially in neuromast hair cells (NM HCs) and crista hair cells (Figure 1B, 1C). Then, NM HCs, supporting cells, and mantle cells were ordered along pseudotime using Monocle 3 (Figure 1D, 1E), and a heatmap was generated to visualize the expression dynamics of marker genes in NM HC (Figure 1F). These data indicate that the expression of *hsd17b7* gene was gradually increased along the NM HC development trajectory (Figure 1D, 1E). Consistently, whole-mount *in situ* hybridization (WISH) in zebrafish showed that *hsd17b7* was specifically enriched in the NM HCs and crista HCs at 72 hours post-fertilization (hpf) and 96 hpf (Figure 1G). To further explore the localization of *hsd17b7* in zebrafish HCs, we generated a *hsd17b7-egfp* fusion construct driven by a hair cell-specific promoter, *myosin 6b* [25, 26]. We injected this construct into a fertilized egg and expressed the *hsd17b7-egfp* fusion in the HCs. Confocal imaging analysis revealed that Hsd17b-EGFP was localized to the cytoplasm in both crista HCs and NM HCs, exhibiting a punctate distribution (Figure 1H, 1I).

Meanwhile, to further elucidate the expression of HSD17B7 in the mammal auditory system, we analyzed the expression levels of Hsd17b7 in three single-cell data sets of the mouse [27-29], we found that Hsd17b7 were highly expressed in outer hair cells (OHCs), utricles hair cells, and inner hair cells (IHCs), but less in crista hair cells (Figure 1J). Next, we assessed the expression of HSD17B7 in C57BL/6 wild-type mice. Immunostaining analysis revealed that HSD17B7 was expressed in both outer hair cells (OHCs) and inner hair cells (IHCs) (Figure 1K), confirming the scRNA-seq data. These results demonstrate that HSD17B7 is highly expressed in the sensory hair cells of zebrafish and mice.

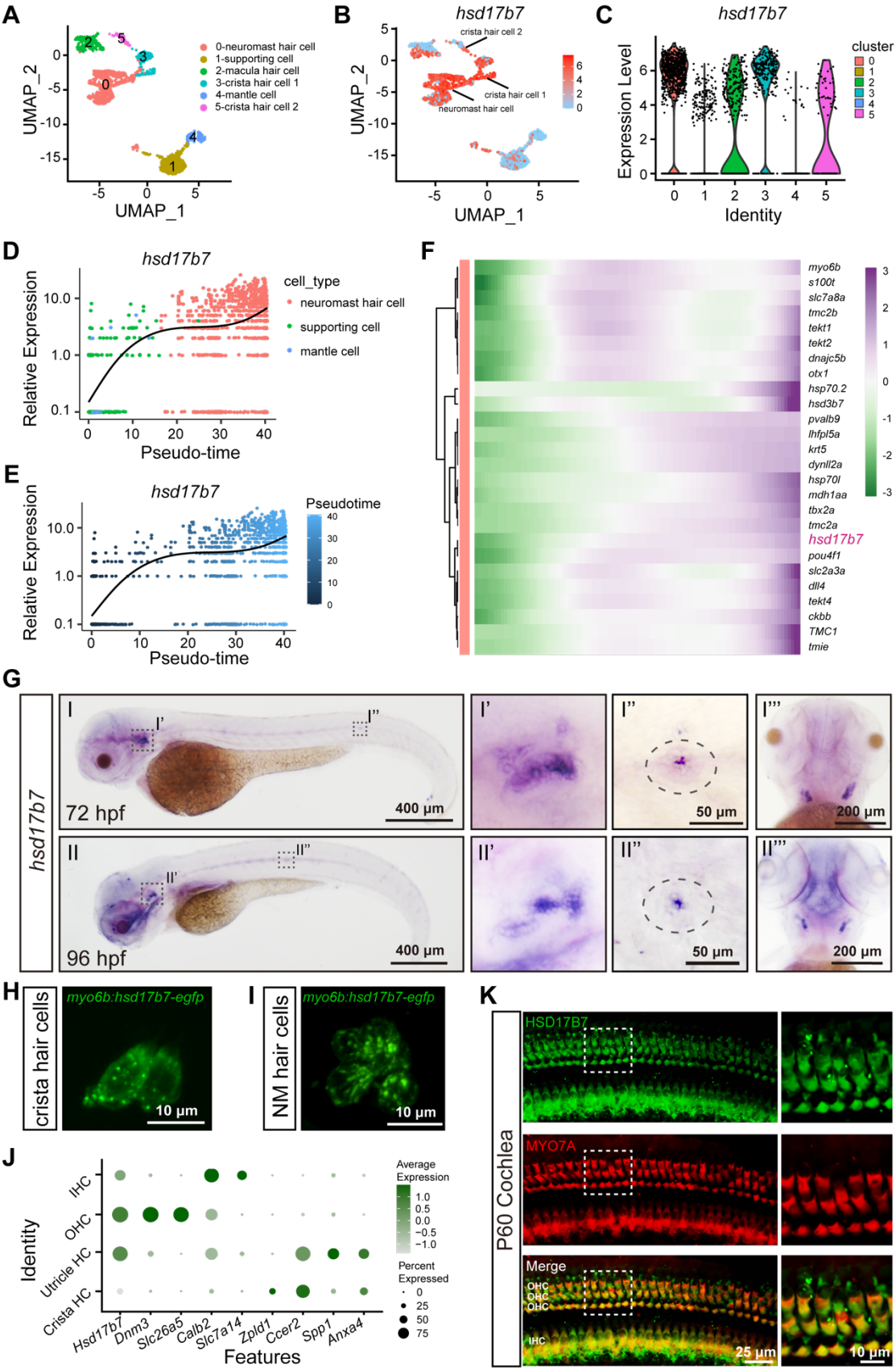

Figure 1. High expression of *HSD17B7* in zebrafish and mice sensory hair cells

(A) The UMAP analysis of the zebrafish scRNA-seq data. 0, 2, 3, and 5 clusters of cells were annotated as hair cells. 0, neuromast hair cell; 1, supporting cell; 2, macula hair cell; 3, crista hair cell 1; 4, mantle cell; 5, crista hair cell 2. (B) and (C) Feature plot and violin plot of *hsd17b7*. (D) *hsd17b7* expression increased along the pseudotime trajectory of neuromast hair cell formation. (E) Increase in *hsd17b7* gene expression levels along the hair cell trajectory. (F) Heatmap of marker genes along the pseudotime trajectory. (G) The expression of the *hsd17b7* in 72 hpf and 96 hpf embryos was detected by whole-mount *in situ* hybridization analysis. Dashed circles indicate the otic vesicle and the neuromast. (H) and (I) Representative images of the crista hair cells and neuromast hair cells in *Tg(myo6b: hsd17b7-egfp)* at 4 dpf. NM hair cells, neuromast hair cells. Scale bars, 10 μm. (J) The average expression of Hsd17b7 and hair cell marker genes across mouse hair cell types. (K) Immunostaining analysis of HSD17B7 expression in mouse cochlea hair cells at P60. MYO7A was used as a marker for hair cells. The dashed box indicates the magnified region. OHC, outer hair cell; IHC, inner hair cell.

In addition, phylogenetic and sequence alignment analysis revealed that vertebrate HSD17B7s share a significant similarity in amino acid sequences (Figure S1A). UniProt sequence alignment analysis revealed that Danio rerio Hsd17b7 (NP_001070796.1) shares 58.2% identity with Homo sapiens HSD17B7 (NP_057455.1) and 67.1% identity with Mus musculus HSD17B7 (NP_034606.3), respectively (Figure S1B). These data suggest that HSD17B7 is conserved and expressed in sensory hair cells across vertebrate species.

Hsd17b7 deficiency impaired auditory and MET function in zebrafish

To investigate the Hsd17b7 function in the auditory system, we generated *hsd17b7* mutant alleles using CRISPR/Cas9-mediated mutagenesis (Figure S2A, S2B). The target site fragment was PCR-amplified and sequenced (Figure S2C, S2D). Sequence analysis revealed that the mutant alleles included a 4-bp deletion and two 6-bp deletions in exon 3 (Figure S2E). Subsequently, the 4-bp deletion mutant line was chosen for further experiments, which led to a reading frame shift and premature termination of protein translation. The mutant protein is predicted to translate to 96 amino acids, then adds 4 code-shifted residues (Figure S2F).

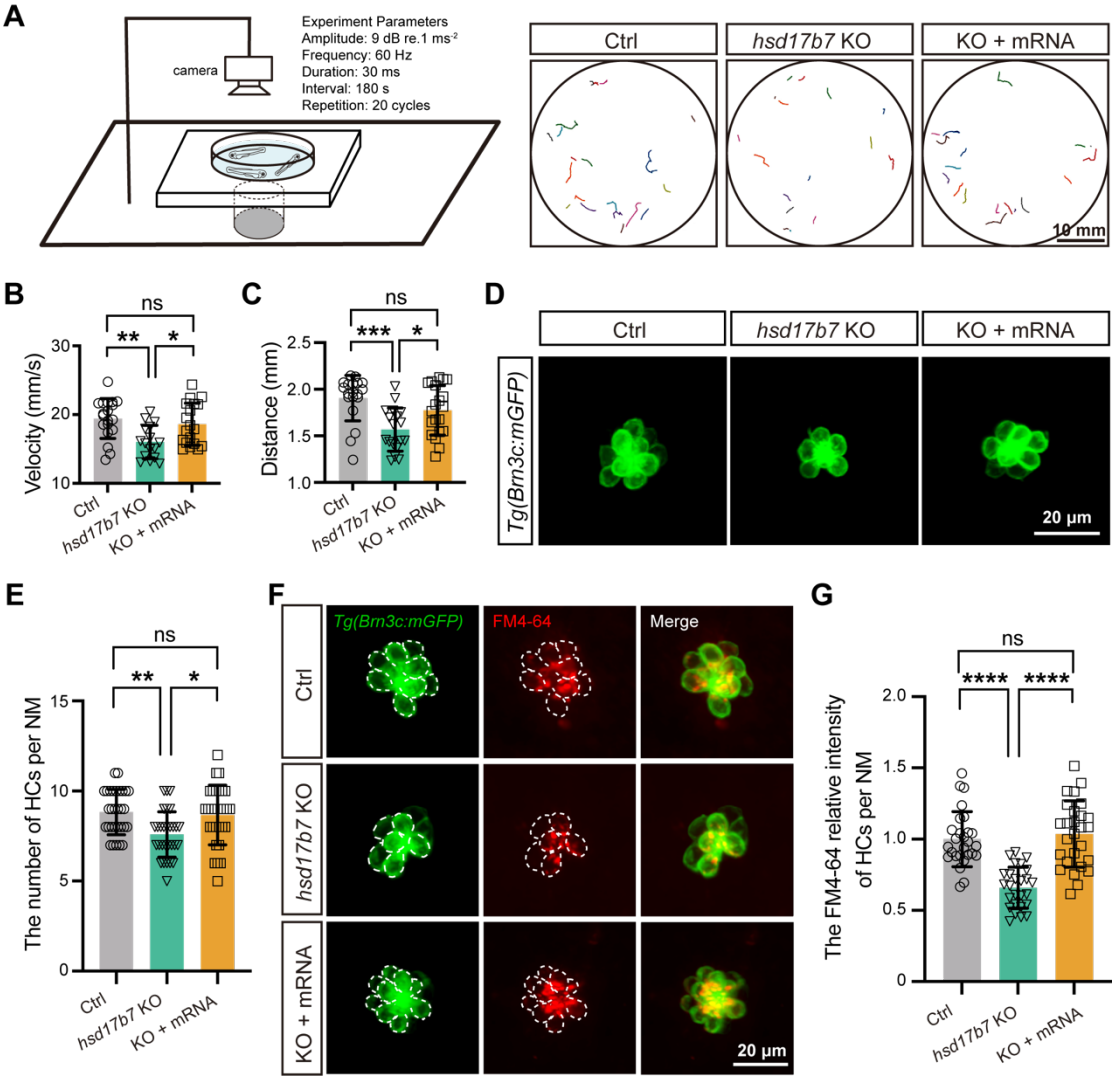

Figure 2. Knockout of *hsd17b7* caused compromised MET function and hearing defects in zebrafish

(A) Left: Schematic diagram of the devices used in the startle response assay applied to larvae. Right: Extracted locomotion trajectories from larvae with C-shape motion under a one-time stimulus of 9 dB re.1 ms^{-2} sound level with 60 Hz tone bursts in control, *hsd17b7* KO, and mRNA rescued groups, respectively. Scale bars, 10 mm. (B) and (C) Quantification of the peak velocity and mean distance of movement at 5 dpf larvae under sound stimuli for (A) (n=20). (D) Representative images of neuromast hair cells (HCs, green) in *Tg(Brn3C: mGFP)* at 4 dpf larvae from control, *hsd17b7* KO, and *hsd17b7* mRNA rescued groups. Scale bars, 20 μm. (E) Quantification of the number of HCs per neuromast for (D) (n=30). (F) Representative images of neuromast HCs (green) and functional HCs (red) in single neuromast of *Tg(Brn3C: mGFP)* at 5 dpf larvae from control, *hsd17b7* KO, and *hsd17b7* mRNA rescued groups, respectively.

The white dashed circles indicate NM HCs. Scale bars, 20 μm. (G) Quantification of the FM4-64 relative intensity of HCs per neuromast for (F) (n=27). All quantification data (B, C, E, and G) are presented as the mean ± SD. P values were determined using a one-way ANOVA test followed by Tukey's multiple comparisons. *P < 0.05; **P < 0.01; ***P < 0.001; ****P < 0.0001; ns, non-significant, p > 0.05.

We first examined the startle response evoked by auditory stimuli to assess the hearing abilities of zebrafish larvae [30]. We found that the movement trajectory, swimming velocity, and distance of the *hsd17b7* mutants were significantly decreased compared to those of the controls at 5 dpf (Figure 2A-2C), indicating that depletion of *hsd17b7* leads to significant hearing loss. To verify that the hearing loss was specifically caused by *hsd17b7* deficiency, we attempted to rescue the impaired auditory function by injecting the *hsd17b7* mRNA into *hsd17b7* mutants. It was shown that the microinjection of *hsd17b7* mRNA successfully restored the compromised movement trajectory, swimming velocity, and distance of the hsd17b7 mutants (Figure 2A-2C), indicating that Hsd17b7 is crucial for the auditory function in zebrafish.

Furthermore, we designed antisense morpholino oligonucleotides (*hsd17b7* Mo) to block the splicing of *hsd17b7* RNA at the junction of exon 1/intron 1 to knock down Hsd17b7 to verify the phenotype (Figure S3A, S3B). RT-PCR revealed that natural *hsd17b7* mRNA expression was significantly reduced, and mis-spliced mRNA was observed after injection of *hsd17b7* Mo (Figure S3C). Additionally, we evaluated the knockdown efficiency and rescue efficiency of *hsd17b7* by immunoblotting. As expected, the protein levels of Hsd17b7 decreased significantly after *hsd17b7* Mo injection, and mRNA injection effectively rescued the Hsd17b7 protein level (Figure S3D). We subsequently found that the movement trajectory, distance, and swimming velocity of the *hsd17b7* morphants were significantly decreased compared to those of controls at 5 dpf (Figure S3E-S3G). Moreover, *hsd17b7* mRNA effectively rescued the defective startle response of *hsd17b7* morphants (Figure S3E-S3G). These results demonstrate that Hsd17b7 is required for auditory function.

Since Hsd17b7 deficiency impaired auditory function, we investigated whether the mechanotransduction (MET) function of Hsd17b7 mutants is compromised. We generated *hsd17b7* mutant alleles in the *Tg(Brn3c: mGFP)* transgenic line [24, 31], in which the membrane of sensory HCs are labeled with GFP. Confocal microscopy imaging analysis revealed that the average number of HCs in *hsd17b7* mutants was decreased compared to that of controls (~16% reduction) (Figure 2D, 2E). FM4-64 (N-(3-Triethylammoniumpropyl)-4-(6-(4-(Diethylamino) Phenyl) Hexatrienyl) Pyridinium Dibromide) is a fluorescence dye that labels HCs and can rapidly permeate HCs through traversing open mechanosensitive channels, which were commonly used as a proxy for MET function in mature HCs [26, 32, 33]. We found that at 5 dpf, the labeling intensity of FM4-64 in the HCs of the lateral line neuromasts in *hsd17b7* mutants was markedly reduced compared with that of controls (~40% reduction) (Figure 2F, 2G). Meanwhile, we also used the FM4-64 staining assay to examine the MET function of *hsd17b7* morphants. The results showed that the FM4-64 intensity in *hsd17b7* morphants was also significantly decreased compared to controls at 5 dpf (~25% reduction) (Figure S4A, S4B). Given that the reduction in HC numbers (~16%) is much smaller than the decrease in FM4-64 labeling intensity (~40%), these results suggest that the loss of *hsd17b7* function primarily affects the MET function of HCs in zebrafish rather than the number of HCs.

To verify that *hsd17b7* is essential for the MET function, we performed a rescue experiment by injecting *hsd17b7* mRNA. It was demonstrated that microinjection of the *hsd17b7* mRNA successfully restored the FM4-64 intensity and the HC numbers (Figure 2D-2G, S4A, S4B). Collectively, these data demonstrate that *hsd17b7* is critical for MET function in zebrafish.

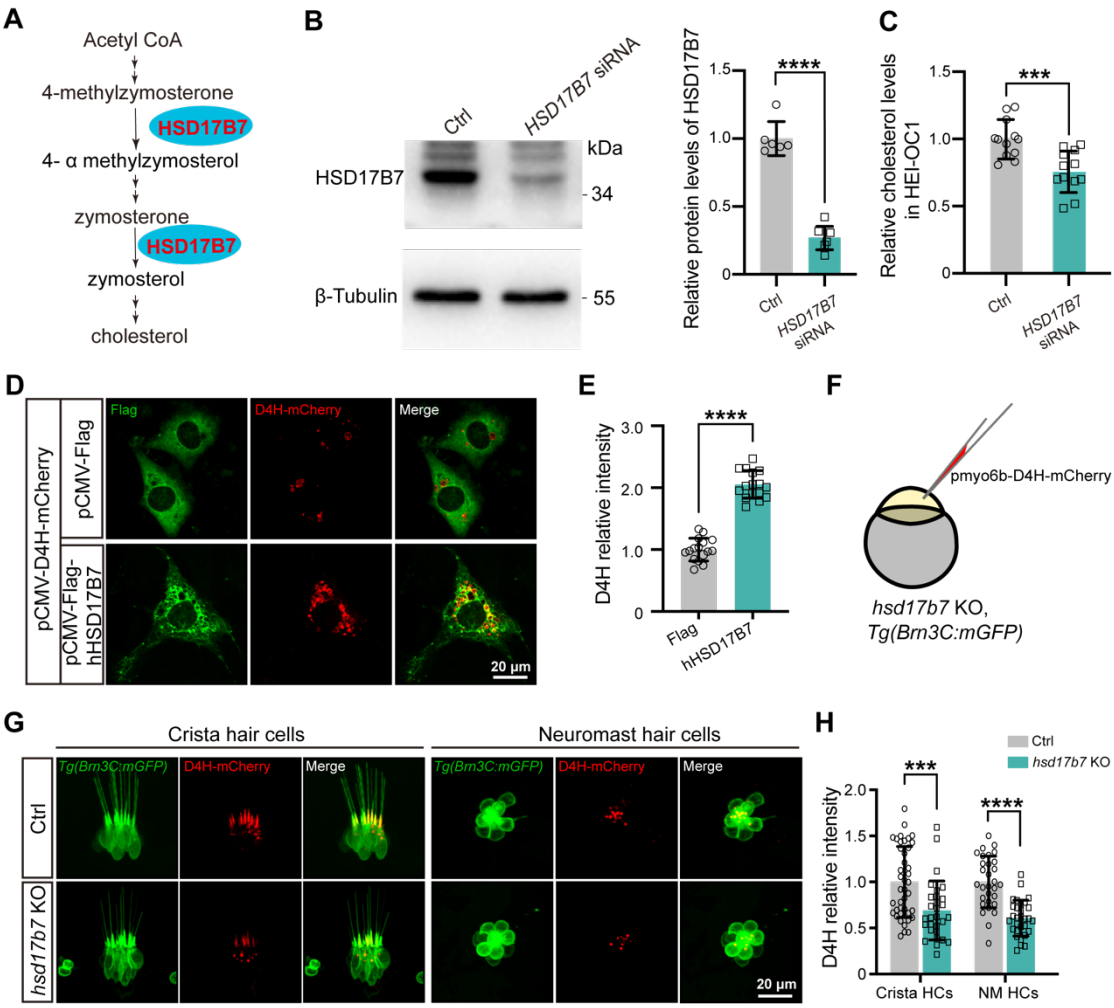

Figure 3. HSD17B7 deficiency reduced cholesterol in hair cells

(A) Schematic representation of the cholesterol synthesis pathway. (B) Western blots showing HSD17B7 protein levels in *HSD17B7* Knock-down HEI-OC1 cells. Quantification of relative protein levels of HSD17B7 is shown on the right (n = 6). (C) Quantification of the relative cholesterol levels in *HSD17B7* knock-down HEI-OC1 cells (n=12). (D) Immunostaining shows cholesterol probe D4H-mCherry in HEI-OC1 cells transfected with pCMV2-Flag and pCMV2-Flag-HSD17B7 full-length plasmids, respectively. Scale bars, 20 μm. (E) Quantification of D4H relative intensity *in vitro* for (D) (n=16). (F) Schematic diagram of *hsd17b7* KO one-cell embryos injection of pmyo6b-D4H-mCherry in *Tg(Brn3C: mGFP)*. (G) Representative images of cholesterol probe D4H-mCherry (red) expression in crista HCs (left) and NM HCs (right) of control or *hsd17b7* KO mutant larvae at 4 dpf. Scale bars, 20 μm. (H) Quantification of D4H relative intensity *in vivo* for (G) (n=30).

All quantification data (B, C, E, and H) are presented as the mean ± SD. P values were determined using a two-tailed unpaired Student's t-test. ***P < 0.001; ****P < 0.0001.

HSD17B7 regulated cholesterol levels *in vitro* and *in vivo*

HSD17B7 converts zymosterone to zymosterol, participating in cholesterol biosynthesis (Figure 3A) [23]. Previous research has indicated that abnormally high and low cholesterol levels are detrimental to hearing [7, 34, 35]. To further explore the physiological mechanism underlying how HSD17B7 affects auditory function, we first verified whether HSD17B7 regulates cholesterol. It was shown that *HSD17B7* knockdown in HEI-OC1 cells led to a decrease in total cellular cholesterol (Figure 3B, 3C). The minimal cholesterol-binding domain 4 (D4H) cholesterol binding probe derived from the toxin Perfringolysin O (PFO) was widely used to monitor cholesterol at the cytoplasmic leaflet of the plasma membrane (PM) [36, 37]. D4H-mCherry was used to monitor the cholesterol in HEI-OC1 cells. Immunostaining results showed that D4H-mCherry intensity was significantly increased in HEI-OC1 cells overexpressing *HSD17B7* compared with control cells (Figure 3D, 3E), suggesting HSD17B7 regulates cholesterol.

To further assess the functional role of Hsd17b7 in regulating cholesterol *in vivo*, we injected the construct expressing D4H-mCherry into one-cell-stage embryos of control and *hsd17b7* mutant *Tg(Brn3c: mGFP)* transgenic line to evaluate the cholesterol in zebrafish (Figure 3F). We found that D4H-mCherry was enriched in the hair bundle (Figure 3G), which is consistent with previous reports [36]. Compared with controls, the intensity of D4H-mCherry in crista HCs and NM HCs of *hsd17b7* mutants at 4 dpf was significantly reduced (Figure 3G, 3H). These results demonstrate that HSD17B7 regulated cholesterol synthesis *in virto* and *in vivo*. Given that abnormal cholesterol homeostasis is detrimental to hearing [7, 34, 35], the deficiency of Hsd17b7 led to compromised MET and auditory function, suggesting that Hsd17b7 regulates auditory function by influencing cholesterol levels in HCs.

A nonsense Variant in *HSD17B7* identified in human deafness

Given the established role of Hsd17b7 in auditory function in zebrafish, the human *HSD17B7* gene was screened in individuals with hearing loss (HL) who remained undiagnosed after analysis of 201 known HL genes using whole-genome sequencing (WGS)[38]. The proband failed the newborn hearing screening, was enrolled in a special education school during early childhood, and presented at 8 years of age with bilateral profound hearing loss. Physical examination revealed two preauricular appendages anterior to the right ear but no other systemic abnormalities. The proband II 1's parents had normal hearing and no family history of HL but declined genetic testing (Figure 4A, 4B). A heterozygous nonsense variant, c.544G>T (p.E182*) in *HSD17B7* (NM_016371.4) was identified and confirmed by Sanger sequencing (Figure 4C). This mutation introduces a premature stop codon at position Glu182 (Figure 4C).

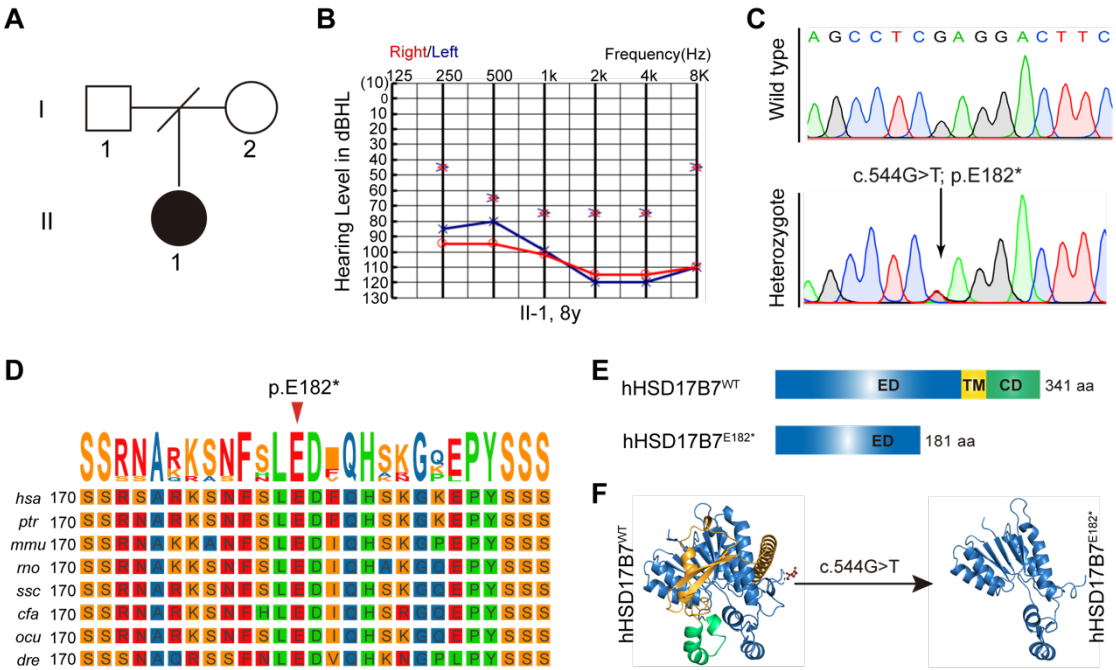

Figure 4. Identification of a novel heterozygote nonsense mutation in *HSD17B7*

(A) Two-generation family pedigree for the affected individual. The hearing-impaired individual is indicated by a black cycle (female). (B) Pure-tone audiometry audiograms for the hearing-impaired individual at 8 years old. Blue represents the results for the left ear and red for the right ear. Affected individual shows severe-to-profound or profound HI. (C) Sequence of HSD17B7 mRNA in Wild type and Heterozygote. (D) Multiple sequence alignment of 8 different species using TBtools program. The p.Glu182 residue as indicated by a red arrow is

evolutionarily conserved from zebrafish to human. (E) The domain structure of human HSD17B7^{WT} and HSD17B7^{E182*}. ED, extracellular domain; TM, transmembrane; CD, cytoplasmic domain. The residue numbers are labeled at right. (F) SWISS-MODEL predicts the three-dimensional protein structure of HSD17B7^{WT} and HSD17B7^{E182*}.

The multiple sequence alignment showed that Glu182 is evolutionarily conserved in eight vertebrates, from zebrafish to humans (Figure 4D), implying that the nonsense mutation may have a potential pathogenetic effect on HI. According to UniProt, the encoded HSD17B7 protein contains two topological domains (extracellular domain: 1-229 aa, cytoplasmic domain: 251-341 aa) and a transmembrane region (230-250 aa). The novel nonsense mutations in the extracellular domain of HSD17B7 (c.544G>T) changed residue 182 from Glu to Ter (p.E182*) and resulted in the production of truncated proteins (Figure 4E). In addition, the three-dimensional protein structure of HSD17B7 is first modeled to predict the effect of the nonsense mutation on the protein using the SWISS-MODEL protein structure database (https://swissmodel.expasy.org) (Figure 4F). This data analysis suggests that this nonsense mutation may have a potential pathogenic effect on hearing loss.

E182* mutation mRNA of HSD17B7 failed to rescue the impaired MET function and auditory behavior of hsd17b7 mutants

To assess the impact of E182* nonsense mutation of HSD17B7 on MET function, we microinjected the human *HSD17B7* wild-type or E182* mutant mRNAs separately into the fertilized one-cell stage embryos of *hsd17b7* KO mutants in *Tg(Brn3c: mGFP)* transgenic line. It was shown that wild-type HSD17B7 significantly increased the FM4-64 intensity in NM HCs of *hsd17b7* mutants, whereas the HSD17B7 E182* mutant mRNA failed to do so (Figure 5A, 5B), indicating that the E182* nonsense mutation of HSD17B7 has no effect in restoring normal MET function in zebrafish. Furthermore, the startle response assay demonstrated that wild-type HSD17B7 successfully rescued the abnormal auditory behaviors (movement trajectory, distance, and swimming velocity) of *hsd17b7* KO mutants, whereas the E182* mutant did not (Figure 5C-5E).

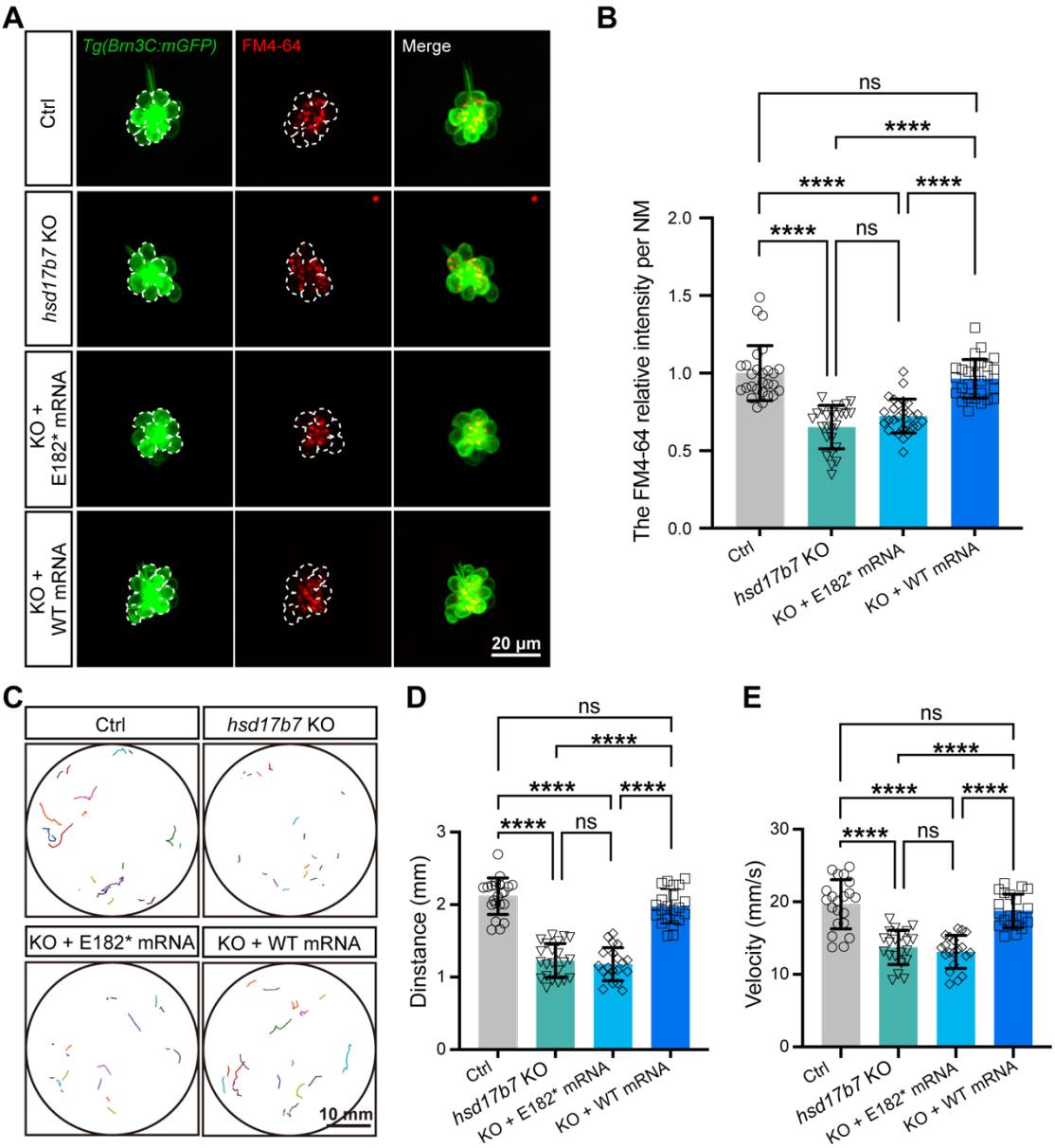

Figure 5. E182* mutation mRNA of HSD17B7 failed to rescue the impaired MET function and auditory behavior of hsd17b7 mutants

(A) Representative images of NM HCs (green) and functional NM HCs (red) in single neuromast of *Tg(Brn3C: mGFP)* at 5 dpf larvae from control, *hsd17b7* KO, KO + E182* mRNA and KO + WT mRNA groups. White dashed circles indicate NM HCs. Scale bars, 20 μm. (B) Quantification of the FM4-64 relative intensity of HCs per neuromast for (A) (n=25). (C) Extracted locomotion trajectories from 5 dpf larvae with C-shape motion under a one-time stimulus of 9 dB re.1 ms-2 sound level with 60 Hz tone bursts in control, *hsd17b7* KO, KO + E182* mRNA, and KO + WT mRNA groups, respectively. Scale bars, 10 mm. (D) and (E) Quantification of the mean distance and peak velocity of movement at 5 dpf larvae under sound

stimuli for (C) (n=20). All quantification data (B, D, and E) are presented as the mean ± SD. P values were determined using a one-way ANOVA test followed by Tukey's multiple comparisons. ****$P < 0.0001$; ns, non-significant, $p > 0.05$.

Heterozygous E182* mutation of HSD17B7 has a negative effect on the auditory function

To explore the pathogenetic role of HSD17B7 E182* heterozygous mutation in the patient's hearing loss, we mimicked the proband II heterozygote *in vitro* and *vivo*. We transiently expressed Flag-tagged HSD17B7 wild-type ($HSD17B7^{WT}$) or E182* nonsense mutation ($HSD17B7^{E182*}$) in HEI-OC1 cells to examine their subcellular localization. Since cholesterol synthesis mainly occurs in the endoplasmic reticulum (ER) [39, 40], we supposed that HSD17B7, an enzyme catalyzing cholesterol synthesis, might localize in the ER. Immunostaining revealed that $HSD17B7^{WT}$ co-localized with Calnexin (an ER marker), whereas $HSD17B7^{E182*}$ did not and instead exhibited a spot-like aggregate distribution (Figure 6A). These results were confirmed by matching fluorescence signal intensity profiles (Figure 6B, 6C). Given that the patient was a heterozygote mutant, we suspected that the $HSD17B7^{E182*}$ mutant might impair the subcellular localization of $HSD17B7^{WT}$. Therefore, we performed immunostaining by co-transfecting HEI-OC1 cells with Flag-$HSD17B7^{WT}$ and $HSD17B7^{E182*}$-Myc expression constructs. The results showed that the presence of the $HSD17B7^{E182*}$ protein did not alter the subcellular localization of $HSD17B7^{WT}$ (Figure 6D), as confirmed by matching two fluorescence signal intensity profiles (Figure 6E).

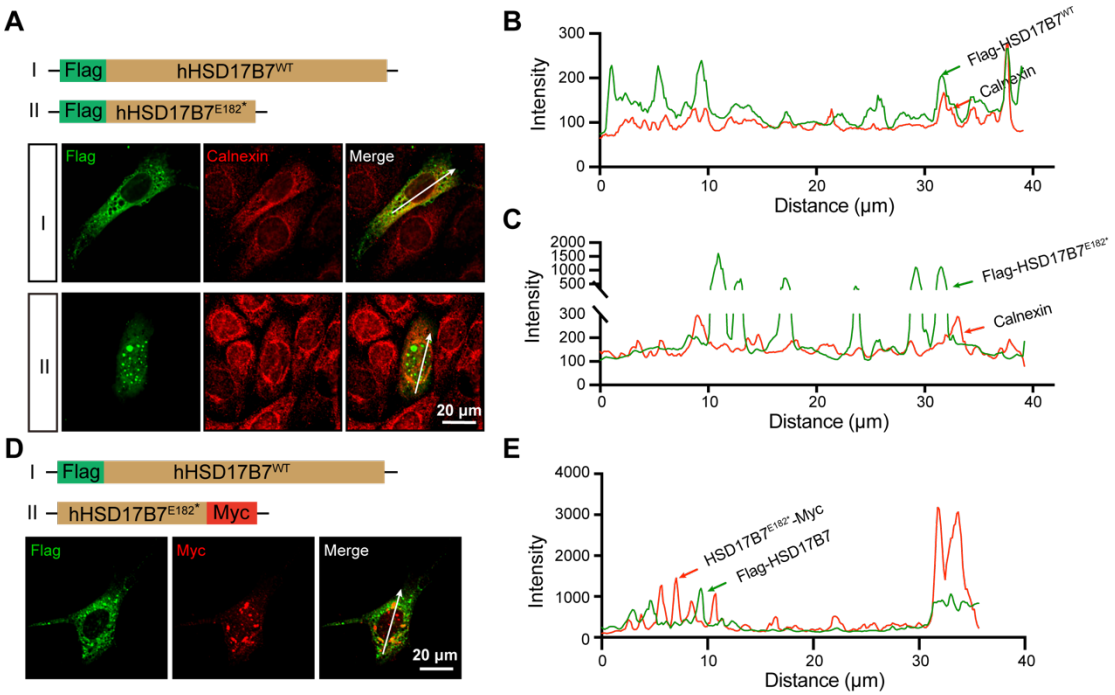

Figure 6. Subcellular localization of HSD17B7 WT and E182* mutation

(A) Immunostaining shows the subcellular localization of Flag-HSD17B7^{WT} and Flag-HSD17B7^{E182*} in HEI-OC1 cells. Calnexin was used as a marker for ER. The white arrow indicates the profile position in (B, and C). Scale bars, 20 μm. (B) and (C) The intensity profile shows the localization of HSD17B7^{WT} and HSD17B7^{E182*} with ER, respectively. (D) Immunostaining shows the subcellular localization of HSD17B7^{WT} and HSD17B7^{E182*} in one HEI-OC1 cell. The white arrow indicates the profile position in (E). Scale bars, 20 μm. (E) The intensity profile shows the localization of HSD17B7^{WT} and HSD17B7^{E182*} in one HEI-OC1 cell.

To further investigate the underlying cause of hearing loss in the patient carrying the heterozygous HSD17B7^{E182*} mutation, we injected human wild-type (HSD17B7^{WT}) or mutant (HSD17B7^{E182*}) *HSD17B7* mRNAs into one-cell stage embryos of the wild-type in *Tg(Brn3c: mGFP)* transgenic line to assess whether the overexpression of HSD17B7^{E182*} impairs MET function and auditory behaviors. The FM4-64 assay revealed that the overexpression of HSD17B7^{WT} did not result in a significant difference in fluorescence intensity compared to the control. In contrast, the overexpression of HSD17B7^{E182*} led to a significant reduction of fluorescence intensity (Figure 7A, 7B). In addition, HSD17B7^{WT} overexpression did not alter the startle response compared to the control. In contrast, HSD17B7^{E182*} overexpression resulted

in abnormal movement trajectory, along with reduced mean distance and peak velocity in response to auditory stimulation (Figure 7C-7E). These data suggest that overexpression of HSD17B7^{E182*} has a negative effect on normal auditory function.

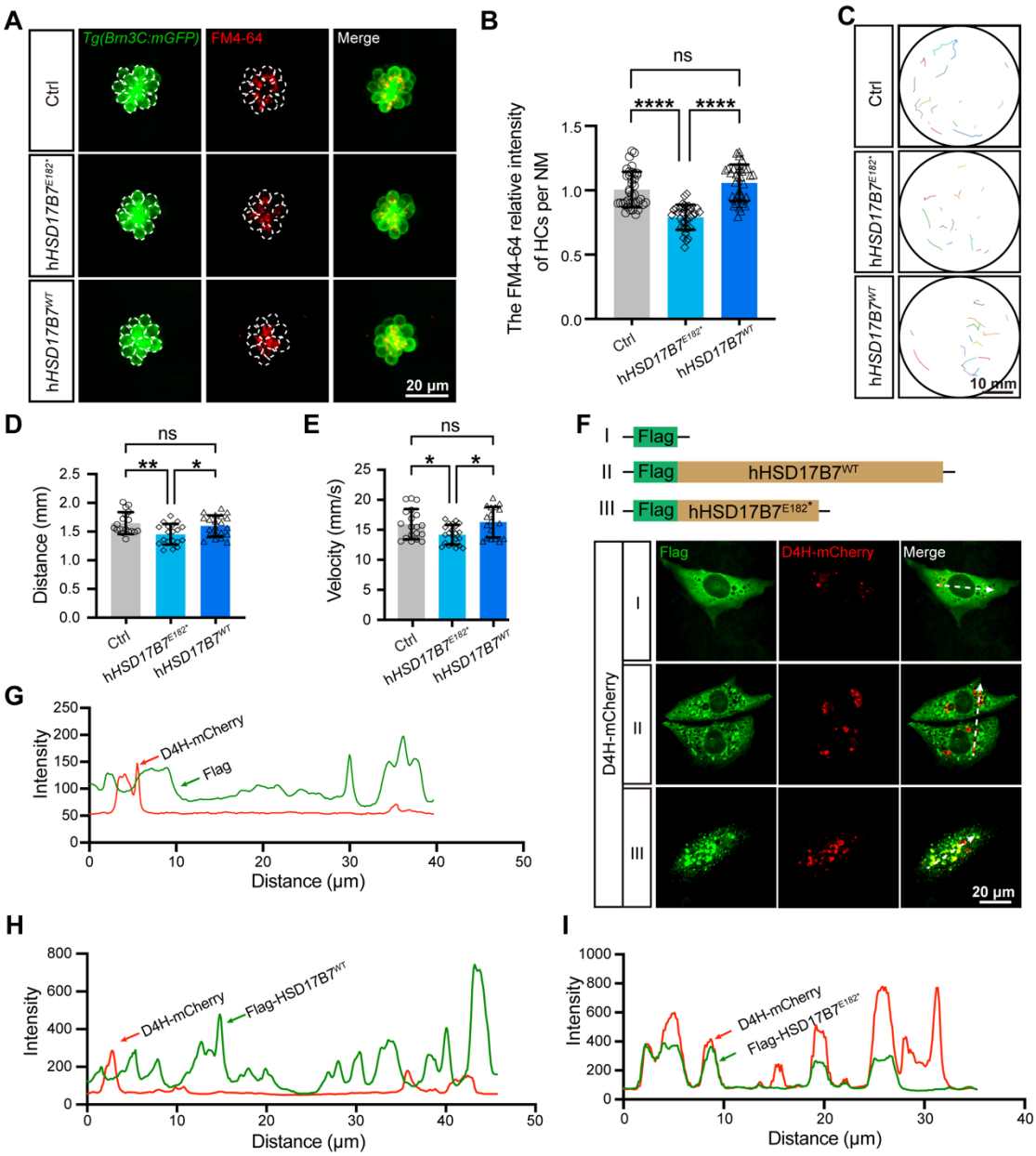

Figure 7. The heterozygous E182* mutation leads to a negative effect on auditory function

(A) Representative images of neuromast HCs (green) and functional HCs (red) in single neuromast of *Tg(Brn3C: mGFP)* at 5 dpf larvae from control, HSD17B7^{E182*} mRNA and HSD17B7^{WT} mRNA groups, respectively. White dashed indicate NM HCs. Scale bars, 20 μm. (B) Quantification of the FM4-64 relative intensity of HCs per neuromast for (A) (n=34). (C) Extracted locomotion trajectories from larvae with C-shape motion under a one-time stimulus

of 9 dB re.1 ms-2 sound level with 60 Hz tone bursts in control, HSD17B7^{E182*} mRNA and HSD17B7^{WT} mRNA groups, respectively. Scale bars, 10 mm. (D) and (E) Quantification of the mean distance and peak velocity of movement at 5 dpf larvae under sound stimuli for (C) (n=20). (F) Immunostaining shows the distribution of cholesterol probe D4H in HEI-OC1 cells transfected with pCMV2-Flag, pCMV2-Flag-HSD17B7^{WT}, and pCMV2-Flag-HSD17B7^{E182*} plasmids, respectively. The white arrow indicates the profile position in (G, H, and I). Scale bars, 20 μm. (G), (H), and (I) The intensity profile shows the localization of Flag, HSD17B7^{WT}, and HSD17B7^{E182*} with the cholesterol probe D4H, respectively. All quantification data (B, D, and E) are presented as the mean ± SD. P values were determined using a one-way ANOVA test followed by Tukey's multiple comparisons. *P < 0.05; **P < 0.01; ****P < 0.0001; ns, non-significant, p > 0.05.

Our studies have shown that HSD17B7 regulates cholesterol in vivo and in vitro (Figure 3), and previous research has demonstrated that proper cholesterol distribution in hair cells is essential for maintaining auditory function [36]. Therefore, we hypothesize that the heterozygous HSD17B7^{E182*} mutation may lead to hearing loss by altering cholesterol distribution. Next, we co-transfected HEI-OC1 cells with Flag, Flag- HSD17B7^{WT}or Flag-HSD17B7^{E182*} constructs along with D4H-mCherry (cholesterol probe). Immunostaining results revealed that in cells expressing Flag or Flag- HSD17B7^{WT}, the cholesterol was distributed in the same way around nuclei. In contrast, the nonsense mutation HSD17B7^{E182*} significantly altered the distribution of D4H-mCherry, forming spot-like aggregation (Figure 7F). Furthermore, HSD17B7^{E182*} colocalized with D4H-mCherry, verified by the fluorescence intensity profile (Figure 7G-7I), suggesting that HSD17B7^{E182*} may bind cholesterol and alter its intracellular distribution. Altogether, these results demonstrate that HSD17B7^{E182*} has a negative effect via altering cholesterol distribution in HCs, leading to compromised MET function and auditory behaviors.

Nonsense mutation (p.E182*) of HSD17B7 disrupted the interaction with RER1 and caused the altered localization and cholesterol distribution

To further explore the pathological mechanism of HSD17B7^{E182*}, we transfected HEI-OC1 cells with Flag, Flag-HSD17B7^{WT,} or Flag-HSD17B7^{E182*} constructs and captured the target proteins by co-immunoprecipitation (Figure 8A). We subsequently performed liquid chromatography-tandem mass spectrometry (LC-MS/MS) analysis of the captured proteins (Figure S5). The proteins that interact with HSD17B7^{WT} and HSD17B7^{E182*}, respectively, are shown in the Venn diagram (Figure 8B). We systematically identified the proteins specifically associated with HSD17B7^{WT} and HSD17B7^{E182*}. Consistent with the role of HSD17B7, proteins specifically associated with HSD17B7^{WT} were strongly enriched for cholesterol metabolic process, while proteins specifically associated with HSD17B7 ^{E182*} were strongly enriched for chromatin remodeling (Figure 8C). Considering that HSD17B7^{WT} and HSD17B7^{E182*} have different subcellular localizations, we examined the cellular component of HSD17B7^{WT}-specific and HSD17B7^{E182*}-specific interacting proteins. It was found that the HSD17B7^{WT}-specific interacting proteins were enriched in the ER, while the HSD17B7^{E182*}-specific interacting proteins were enriched in the nucleus and cytoplasm (Figure 8D), consistent with the immunostaining results (Figure 6A-6C). Among these ER-associated proteins, RER1 has the top hit (Figure 8E). RER1 is involved in protein retention in ER [41, 42]. We verified the direct interaction between HSD17B7^{WT} and RER1 by an *in vitro* binding assay. Glutathione S-transferase (GST)-HSD17B7, but not GST, is bound directly to RER1 fused His (RER1-His) (Figure 8F). Next, we co-transfected HEI-OC1 cells with RER1-Myc along with Flag-HSD17B7^{WT} or Flag-HSD17B7^{E182*} constructs. The immunostaining results indicated that RER1 co-localized with HSD17B7^{WT}, whereas it did not co-localize with HSD17B7^{E182*} (Figure 8G), as confirmed by the intensity profiles (Figure 8H, 8I). These data demonstrate that RER1 interacts with HSD17B7^{WT} but not with HSD17B7^{E182*}, suggesting that the localization of HSD17B7^{WT} in the ER is due to its interaction with RER1. In contrast, HSD17B7^{E182*} cannot interact with RER1, resulting in abnormal subcellular localization.

During transfection of Flag-HSD17B7^{WT} and Flag-HSD17B7^{E182*} constructs in HEI-OC1 cells, we noticed that the number of positive cells expressing HSD17B7^{E182*} was very low (Figure S6A). Additionally, the IP results also suggested that the nonsense mutation E182* in HSD17B7 led to a significant decrease in protein levels compared to HSD17B7^{WT} (Figure 8A).

To explain the phenomenon, we transfected equal amounts of Flag-HSD17B7^{WT} and Flag-HSD17B7^{E182*} constructs to confirm their protein levels. Immunoblotting revealed that the levels of E182* mutation protein were significantly lower compared to those of the wild-type (Figure S6B), consistent with our aforementioned findings. Next, we measured the mRNA level of HSD17B7^{WT} and HSD17B7^{E182*}. RT-qPCR results showed that the mRNA levels of the E182* mutation were significantly lower compared to those of the wild-type (Figure S6C). Considering that the E182* mutation decreased not only the protein levels but also the mRNA levels, we subsequently examined the effect of the mutation on the half-life periods of mRNA (Figure S6E). Interestingly, the E182* mutation shortened the mRNA half-life periods of *HSD17B7* (Figure S6D). Overall, the E182* mutation reduced the stability of *HSD17B7* mRNA, resulting in significantly decreased mRNA and protein levels. The abnormally low levels of HSD17B7^{E182*} cannot bind with RER1, preventing proper localization of HSD17B7 to the ER. This, in return, disrupts cholesterol synthesis and distribution, resulting in abnormalities in MET function and auditory behaviors.

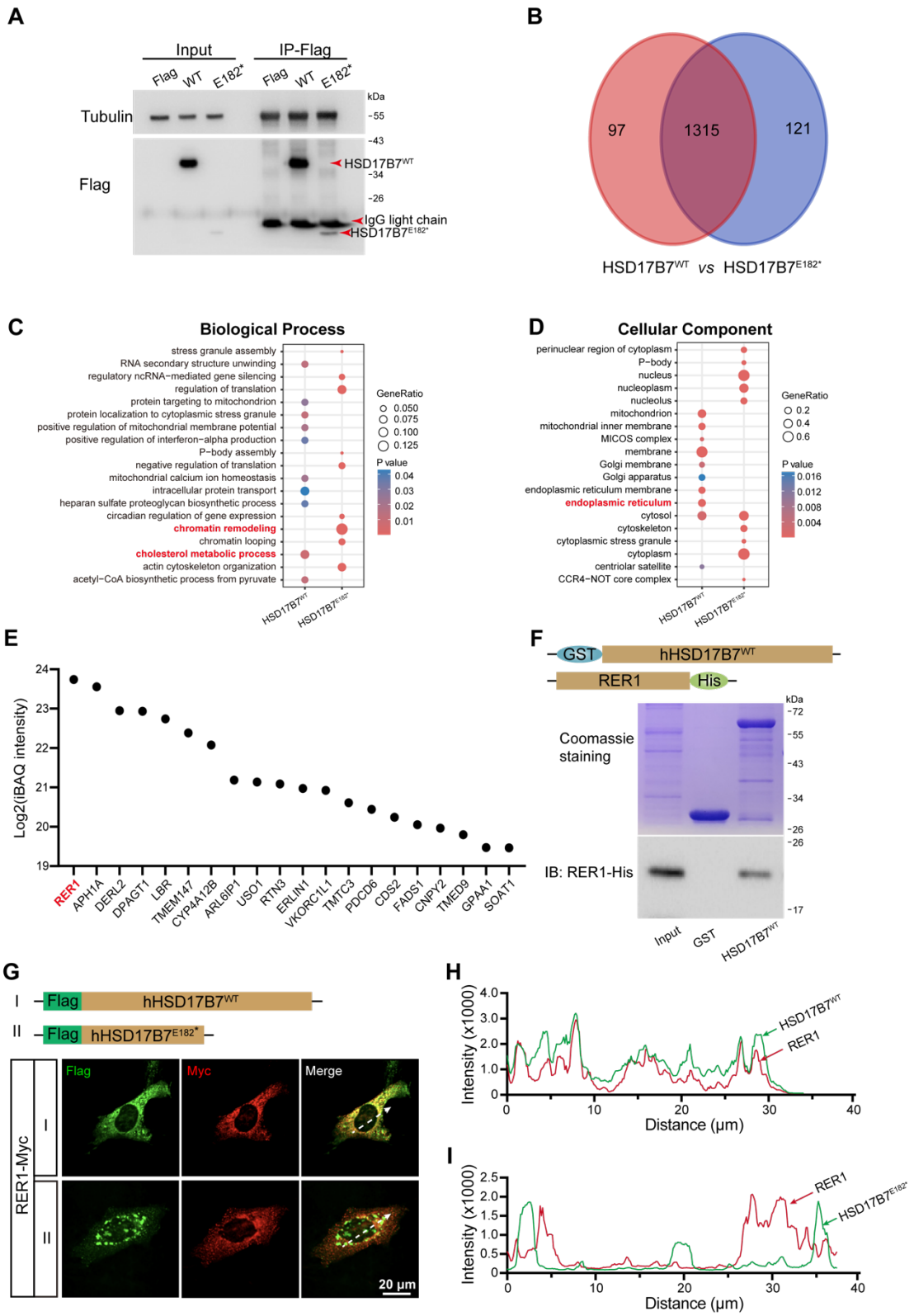

Figure 8. HSD17B7^{WT} binds with Retention in endoplasmic reticulum 1 (RER1)

(A) Flag, Flag-HSD17B7^{WT}, and Flag-HSD17B7^{E182*} were immunoprecipitated from HEI-OC1 cells transfected with pCMV2-Flag, pCMV2-Flag-HSD17B7^{WT}, and pCMV2-Flag-HSD17B7^{E182*} plasmids, respectively. Tubulin and IgG light chains were used as the loading

control. Cell lysates were immunoprecipitated with anti-Flag beads. (B) The Venn diagram shows the number of HSD17B7^{WT} interacting proteins (red) and HSD17B7^{E182*} interacting proteins (blue) identified in LC-MS/MS. The number of proteins in each area is marked. (C) Biological Process GO term enrichment analysis for the HSD17B7^{WT}-specific interacting proteins and HSD17B7^{E182*}-specific interacting proteins identified in LC-MS/MS. (D) Cellular Component GO term enrichment analysis for the HSD17B7^{WT}-specific interacting proteins and HSD17B7^{E182*}-specific interacting proteins identified in LC-MS/MS. (E) The top 20 (iBAQ intensity) for the HSD17B7^{WT}-specific interacting proteins in the ER. (F) *In vitro* binding assays show the interaction between HSD17B7 and RER1. Top: GST and GST-HSD17B7 used for the pull-down assay were stained with Coomassie blue. Bottom: Western blot for RER1-His. (G) Immunostaining shows the localization of RER1-Myc in HEI-OC1 cells transfected with pCMV2-Flag-HSD17B7^{WT} and pCMV2-Flag-HSD17B7^{E182*} plasmids, respectively. The white arrow indicates the profile position in (H, and I). Scale bars, 20 μm. (H) and (I) The intensity profile shows the localization of HSD17B7^{WT} and HSD17B7^{E182*} with RER1, respectively.

Discussion

This study reveals that HSD17B7 is enriched in sensory hair cells in zebrafish and mice, regulating cholesterol levels in hair cells, and is essential for normal mechanotransduction and auditory function. Loss of *hsd17b7* markedly reduces cholesterol in hair cells, causing abnormal MET function and hearing behaviors, suggesting that HSD17B7 is a novel candidate gene for sensory hearing loss. This was further supported by a case of sporadic deafness, in which we identified a previously undescribed variant (c.544G>T, p.E182*) in *HSD17B7* through whole-exome sequencing and Sanger sequencing analyses. The residual HSD17B7^{E182*} protein alters subcellular localization and disrupts normal cholesterol distribution. The E182 mutation in HSD17B7 reduces the mRNA half-life, decreases mRNA abundance, and significantly lowers protein expression levels. Collectively, our findings suggest that the heterozygous c.544G>T (p.E182*) in the HSD17B7 (NM_016371.4) gene disrupts auditory function through potential pathogenic mechanisms. First, the heterozygous E182* mutation altered the intracellular distribution of cholesterol. Second, the haploinsufficiency resulting from reduced HSD17B7 protein levels disrupts cholesterol biosynthesis. These mechanistic insights highlight the critical role of cholesterol homeostasis in auditory function, providing a molecular basis for the development of potential targeted therapeutic strategies.

HSD17B7 was first identified in the rat prolactin receptor-associated protein [43], which is thought to play a key role in the production of estradiol E2 [44, 45]. Subsequent *in vitro* experiments demonstrated that HSD17B7 participated in cholesterol synthesis by catalyzing the reduction of zymosterone to zymosterol [46-48]. Both *in vivo* and *in vitro*, a deficiency of HSD17B7 leads to decreased cholesterol levels, while overexpression of HSD17B7 results in increased cholesterol levels, consistent with the pathway of cholesterol synthesis. Previous studies have shown that HSD17B7 is expressed in the liver, heart, brain, eye, and ear [22, 23, 49]. Although the role of the *HSD17B7* gene in ovarian and breast cancer has been extensively explored in the literature [50-54], the role of the *HSD17B7* gene in auditory function remains unclear. Our study highlights that HSD17B7 is essential for normal hearing in vertebrates. This conclusion is supported by the high expression of HSD17B7 in sensory hair cells across

vertebrate inner ears, as revealed by the results of whole-mount *in situ* hybridization and immunostaining in our current study, as well as single-cell RNA sequencing data from our previous publication and those of others [24, 27-29]. Given that loss of *hsd17b7* causes abnormal hearing behaviors, our research identifies HSD17B7 as a novel candidate gene for sensory hearing loss.

Cholesterol is a component of biological membranes, and it plays both structural and functional roles in the bio-membranes [55, 56]. Previous studies have shown that abnormally high or low cholesterol levels, or abnormal cholesterol distribution, are detrimental to the auditory system [7, 10, 11, 34-36, 57, 58]. However, they have not explored the effect of cholesterol synthesis by hair cells on this system. Smith–Lemli–Opitz syndrome (SLOS) is a common autosomal recessive disorder caused by mutations in the DHCR7 gene. It is characterized by multiple congenital malformations and intellectual disability resulting from an inborn error of cholesterol synthesis. The syndrome exhibits a wide spectrum of manifestations, ranging from mild behavioral and learning difficulties to perinatal lethality. Additionally, patients commonly present with sensorineural hearing loss; however, auditory function has not been thoroughly investigated [59]. Our study revealed that HSD17B7, an enzyme involved in cholesterol synthesis, is enriched in sensory hair cells and regulates cholesterol levels in these cells, playing a crucial role in maintaining normal auditory function. We found that knocking down or knocking out HSD17B7 resulted in low cholesterol levels, leading to auditory deficiency, whereas overexpressing HSD17B7, which caused elevated cholesterol, did not affect auditory behaviors. Given that the stereocilia links of hair cell kinocilia require cholesterol anchoring, we hypothesize that the hair cell function requires cholesterol to maintain a minimum critical concentration. Cholesterol may stiffen biological membranes [60], a biophysical feature that can be directly involved in MET [61, 62]. Conserved protein-lipid interactions in the TMC1 and TMC2 complex structures of MET-related proteins have been highlighted by cryo-EM [63, 64]. Our research found the truncated variant HSD17B7^{E182*} disturbed cholesterol abundance and distribution *in vitro*. Considering that the absence of Hsd17b7 or the overexpression of HSD17B7^{E182*} can lead to abnormal MET function *in vivo*, we hypothesized that HSD17B7 might regulate MET function by affecting the abundance or distribution of cholesterol in hair

cells. Our study suggests that cholesterol might regulate hearing function by affecting MET function. Therefore, how cholesterol abnormalities caused by HSD17B7 deficiency or mutations regulate MET function requires further investigation.

Dominant non-syndromic hearing loss is common in patients with hereditary deafness [65-72]. Typically, the dominant allele is inherited from one parent, and *de novo* mutations should be considered in all cases with a negative family history. Considering that the parents of the proband II 1 had normal hearing but were not willing to provide blood samples for sequencing analysis, and combined with the Sanger sequencing analysis of the proband II 1, it can be inferred that the proband II 1 may have *de novo* dominant non-syndromic hearing loss. However, this conclusion requires further confirmation through additional clinical cases. Some examples of dominant-negative effects in deafness have been reported, such as *KCQN4* and *GJB2* [73-76]. Here, we report a case of sporadic deafness with an *HSD17B7* (c.544G>T, p.E182*) heterozygous mutation, characterized by bilateral profound deafness with no other clinical features. We found that the mRNA of *HSD17B7* (c.544G>T, p.E182*) could not rescue the abnormal auditory function caused by the *hsd17b7* KO in a zebrafish. Interestingly, the overexpression of the *HSD17B7* mutant mRNA in wild-type zebrafish impaired auditory function, indicating that this nonsense mutation has a negative effect. Our results suggest that the $HSD17B7^{E182*}$ mutant may be due to the altered cholesterol distribution.

In conclusion, we demonstrated that Hsd17b7 is required for auditory function by regulating cholesterol synthesis in sensory hair cells. Hsd17b7 deficiency leads to cholesterol abnormalities, disrupting the MET and auditory function. Additionally, we identified a sporadic nonsense mutation in the *HSD17B7* gene in patients with deafness. Our research provides new insights into the critical role of cholesterol in hearing preservation and lays a molecular function for targeted therapeutic strategies.

Acknowledgments

This work was supported by the National Natural Science Foundation of China Grants (32200783 to Y.Q.S; 92368104 and 32350017 to D.L.) and the Natural Science Foundation of Jiangsu Province Grants (BK20220607 to Y.Q.S).

Author Contributions

Conceptualization, Y.Q.S., Z.Y.W., and D.L.; methodology, Y.Q.S., Z.Y.W., M.J.Z., Xu.W., F.P.Q.; investigation, Y.Q.S., Z.Y.W., and D.L.; writing - original draft, Y.Q.S., Z.Y.W., Xi.W., and D.L.; writing - review & editing, Y.Q.S., Z.Y.W., and D.L.; funding acquisition, Y.Q.S., and D.L.; resources, Z.M.J., and J.C.; supervision, D.L and J.C.

Declaration of interests

The authors declare no competing interests.

Resource and Data Availability

The plasmids and zebrafish lines generated in this study are available on request to the Lead Contact. The published article includes all datasets generated or analyzed during this study. Any additional information required to reanalyze the data reported in this paper is available from the Lead Contact upon request.

Materials and Methods

Mouse and zebrafish husbandry

For mouse husbandry, mice in the C57BL/6J background were purchased from the Laboratory Animal Center of Nantong University. Mice were maintained in a barrier facility at 25°C on a regular 12-hours light and 12-hours dark cycle. The day of vaginal plug observation was embryonic day 0.5 (E0.5), and the day of birth was considered postnatal day 0 (P0). For zebrafish husbandry, zebrafish (*Danio rerio*) were raised and maintained at 28.5°C. Wild-type AB zebrafish line and the transgenic zebrafish line *Tg(Brn3c: mGFP)* were used in the study described in our previous study [77]. The embryonic stage is defined as described in the literature [78]. Embryos were collected after natural spawns and moved to E3 medium (5 mM NaCl, 0.17 mM KCl, 0.33 mM $CaCl_2$, and 0.33 mM $MgSO_4$, pH 7.2). After 20 hours post-fertilization (hpf), embryos were moved to a medium containing 0.2 mM phenylthiourea (PTU) to prevent pigmentation for *in situ* hybridization and imaging. All animal experiments were performed under the guidelines of the Institutional Animal Care and Use Committee of Nantong University.

Cell culture

Mice HEI-OC1 were obtained from Prof. Renjie Chai. The cells were authenticated by short tandem repeat (STR) profiling (Shanghai Biowing Applied Biotechnology Co., Ltd). The cell lines were routinely tested negative for mycoplasma using the MycoBlue Mycoplasma Detection Kit (Vazyme Biotech, #D101-01), and cell aliquots from early passages were used. HEI-OC1 cells were cultured in DMEM (Wisent, #319-005-CL) medium supplemented with 10% FBS (Sigma-Aldrich, #F8318) in an incubator with 10% CO_2 at 33°C.

Human HEK293T (sex unknown) cells were obtained from the Shanghai Institute of Biochemistry and Cell Biology (SIBC) and authenticated by short tandem repeat (STR) profilin (Shanghai Biowing Applied Biotechnology Co.,Ltd). The cell lines were routinely tested negative for mycoplasma using the MycoBlue Mycoplasma Detection Kit (Vazyme Biotech, #D101-01), and cell aliquots from early passages were used. Cells were cultured in DMEM (Wisent, #319-005-CL) medium supplemented with 10% FBS (Sigma-Aldrich, #F8318) in an incubator with 5% CO_2 at 37°C.

Antibodies

Anti-MYO7A (1:150, Developmental Studies Hybridoma Bank, #138-1); anti-HSD17B7 polyclonal antibody (1:150-1:1000, proteintech, #14854-1-AP); anti-MYC tag polyclonal antibody (1:200, proteintech, #16286-1-AP); anti-His antibody (1:2500， proteintech, # 66005-1-Ig); anti-DYKDDDDK tag mouse monoclonal antibody (1:200-1:5000, proteintech, #66008-4-Ig); anti-calnexin polyclonal antiboy (1:100, proteintech, #10427-2-AP); tubulin monoclonal antibody (1:5000, proteintech, #66031-1-Ig); goat anti-rabbit IgG(H+L) HRP (1:5000, MULTI SCIENCES, #GAR007); goat anti-mouse IgG(H+L) HRP (1:5000, MULTI SCIENCES, #GAM007); FITC goat anti-mouse IgG (H+L) (1:200, ABclonal, #AS001); Cy3 goat anti-rabbit IgG (H+L) (1:200, ABclonal, #AS007); anti-Digoxigenin-AP Fab fragments (1:1000, Roche, #11093274910).

RNA Isolation, Reverse Transcription (RT), and Quantitative Real-time PCR (RT-qPCR)

Total RNAs of all samples were extracted using TRIzol reagent (Invitrogen, #15596026), and genomic DNA contamination was removed by DNase I (Vazyme, #EN401) following the manufacturer's directions. The RNA yield was determined using NanoDrop ND-2000 (Thermo Fisher Scientific, USA), and integrity was checked on a 1% agarose gel.

The cDNA was synthesized by using HiScript III RT SuperMix (Vazyme, #R323-01) following the manufacturer's directions. Subsequently, quantitative PCR was performed using the ChamQ SYBR qPCR Master Mix (Vazyme, #Q341-02) with the specified primers (*HSD17B7* primer, F: 5'- GACAAGCTTGGATCCATGCGAA -3', R: 5'-ACCTGGACAATGGTGACCTC -3'; *Gapdh* primer, F: 5'-CACAGTCAAGGCCGAGAATGGGAAG-3', R: 5'-GTGGTTCACACCCATCACAAACATG) with a final volume of 20 μL under the following condition: 15 min at 50°C, 5 min at 95°C, and then 40 cycles at 95°C for 15 s and 60°C for 30 s. Relative expression levels for the *Hsd17b7* gene were calculated using the $2^{-\Delta\Delta CT}$ method, normalized to the *Gapdh.* All reactions were repeated in triplicate for each sample. The results were analyzed using the GraphPad Prism software (version 9.4.0).

Whole-mount in situ hybridization and image acquisition

The whole-mount in situ hybridization (WISH) of zebrafish was performed according to the following standard procedures. A 403 bp cDNA fragment of zebrafish *hsd17b7* gene was amplified via PCR using designed primers (F: 5'-GACGTCCTCCAGTAATGCCC-3', R: 5'-CATCTTGCTTGGTCGGGTGT-3') and was cloned into the pGEM-T-easy vector. After linearization of the pGEM-T-easy vector inserting the *hsd17b7* fragment, the DIG RNA Labeling Kit (SP6) (Roche, #11175025910) was used to prepare digoxigenin-labeled *hsd17b7* antisense mRNA probes through transcription *in vitro*. Subsequently, embryos at different developmental stages were hybridized with an *hsd17b7* mRNA probe overnight after a series of treatments, including fixation in 4% paraformaldehyde in PBS, digestion in proteinase K (Roche, #3115879001), and incubation with a pre-hybridized mix. Finally, the alkaline phosphatase (AP)-conjugated antibody against digoxigenin (Roche, #11093274910) and the AP-substrate NBT/BCIP solution (Roche, #11681451001) were used to detect the *hsd17b7* expression. The WISH images of zebrafish were acquired using a stereomicroscope (Olympus, MVX10, Japan).

Plasmids construction

The HSD17B7^{WT} and RER1 full-length cDNAs were PCR amplified from the HEK293T cDNA and cloned into the pGEX-TEV and pET-23b vector, respectively. HSD17B7^{E182*} was generated by site-directed mutagenesis. For cell transfection, the cDNA of HSD17B7^{WT} and HSD17B7^{E182*} were subcloned into the pCMV2-Flag vector, respectively. The cDNA of RER1 and HSD17B7^{E182*} were subcloned into the pcDNA3.1-Myc-His A vector, respectively. eGFP was subcloned into pCMV2-Flag-HSD17B7^{WT} and pCMV2-Flag-HSD17B7^{E182*}, respectively. pCS2-D4H-mCherry was obtained from G. Peng's lab. For plasmid injection of zebrafish, myosin 6b promoter was subcloned into the p-mTol2 vector, followed by D4H-mCherry was subcloned into the p-mTol2 vector. The cDNAs encoding the human protein of HSD17B7^{WT}-eGFP and HSD17B7^{E182*}-eGFP were inserted into the p-mTol2-myo6b vector, then linking P2A-D4H-mCherry by overlap extension. For mRNA injection of zebrafish, the cDNAs encoding the human protein of HSD17B7^{WT} and HSD17B7^{E182*} were inserted into the pCS2^{+}

and likewise, the cDNAs encoding the zebrafish full-length protein of Hsd17b7 were inserted into the pCS2^{+}, which were linearized using NotI and then transcribed in vitro to generate mRNA. All constructs were verified by DNA sequencing.

Cell transfection

HEI-OC1 cells were transfected with plasmids using an X-treme GENE HP DNA transfection reagent (Roche, #6366236001) according to the manufacturer's protocol. After 36 hours or 48 hours transfection, the cells were fixed or collected and subjected to further analyses, including western blots, Co-IP, IF, or RT-qPCR.

HEI-OC1 cells were transfected with small interfering RNA. The mouse *Hsd17b7* siRNA oligos (F: 5'-GGAGGUGUUUGAAACCAAUTT-3', R: 5'-AUUGGUUUCAAACACCUCCTT-3') were synthesized from GenePharma (Shanghai, China). Cells were transfected with siRNA oligos to knock down mHSD7B7 using Lipofectamine RNAiMAX (Invitrogen, #13778-150) according to the manufacturer's protocols. Approximately 1×10^{5} cells per well were placed in six-well plates. When the cell density reached 70-80%, 4 μL of control siRNA or mHsd17b7 siRNA were added to 150 μL of opti-MEM (Gibco, #31985070), then 5 μL Lipofectamine RANiMAX was added, incubated at room temperature for 5 min, then added them to the cell culture medium. After 48 hours transfection, the transfected cells were harvested for western blots or cholesterol assay.

mRNA stability assay

HEI-OC1 cells were transfected with plasmids using an X-treme GENE HP DNA transfection reagent. After 24 hours, the cells were treated with 10 μM actinomycin D (MCE, #HY-17559) for 0, 2, 4, 6 and 8 hours. Then collected cells and isolated RNA for RT-qPCR [79].

Immunostaining and image acquisition

Cultured cells grown on coverslips, after 36 hours transfection, cells were fixed with 4% paraformaldehyde in PBS for 30 min at room temperature and washed 3 times with PBS, then followed by permeabilized in 0.3% PBST (0.3% Triton X-100 in PBS) for 20 min. After three times washes with PBS, the cells were blocked with 10% FBS in PBS, followed by incubation

with anti-primary antibodies overnight at 4°C, and then incubated with fluorescent dye-labelled secondary antibodies for 2 hours at room temperature before mounting using the mounting solution with DAPI (1:500, SouthernBiotech, #011-20).

The dissected mouse cochleae were fixed with 4% paraformaldehyde in PBS for 1 hours at room temperature. After 3 times washes with 0.1% PBST, the cochleae were briefly blocked with a blocking medium (PBS containing 1% Triton X-100 and 10% heat-inactivated donkey serum, pH 7.2) for 1 hours at room temperature, followed by incubation with the anti-primary antibody overnight at 4°C. Then the samples were washed in 0.1% PBST and incubated with the fluorescent dye-labelled secondary antibodies for 2 hours at room temperature before mounting using the mounting solution with DAPI (1:500, SouthernBiotech, #011-20).

The immunostaining images of stained HEI-OC1 cells and cochlea were acquired by a Nikon confocal microscope with NIS-Elements software. For zebrafish live imaging, the larvae were anesthetized with tricaine MS-222 (Sigma, #A5040) and mounted in 0.6% low-melting agarose (Invitrogen, #16520050) with a lateral view. All the reconstructed three-dimensional images and adjusted contrast were used with Imaris X64 software (version 9.0.1).

FM4-64 labeling

To investigate the basal activity of neuromast hair cells, the FM4-64 (1:500, Invitrogen, #T13320) vital dye was used to specifically label functional HCs in the neuromasts. The staining procedures were carried out as described previously [25, 26, 32, 33]. The free-swimming larvae were incubated in 3 μM FM4-64 vital dye for 15 s at room temperature in the dark. Afterward, the fish were rinsed 3 times using a PTU medium and imaged. The images of stained hair cells were acquired by a Nikon confocal microscope with NIS-Elements software.

Measurement of total cholesterol

HEI-OC1 cells were homogenized in chloroform/methanol (2:1) to extract lipids and then centrifuged at 20,000 × *g* for 10 min. The organic phase was harvested and dried using nitrogen flow. Total cellular cholesterol was quantified using an Amplex Red cholesterol assay kit (Invitrogen, #A12216) through a multilabel reader (PerkinElmer, USA) according to the manufacturer's instructions.

Morpholino and mRNA injections

For inhibiting the expression of *hsd17b7*, *hsd17b7*-specific splicing-blocking morpholinos were designed and procured from Gene Tools, Inc. and the precise sequence was (5'-TGCAAACAGGTAACAAAACTGTGTG-3'). The powder of morpholino was dissolved and diluted in RNase-free water to obtain the work solution with a 0.3 mM final concentration for subsequent operations. About 2 nL dose of morpholino work solution was microinjected into zebrafish embryos at the one-cell stage. To examine the morpholino efficiency, embryos injected with morpholino were collected to extract RNA which then was subjected to reverse transcript cDNA. The designed primers franking on exon 1 and exon 2 (F: 5'-TACACAGGCAAACGTTAGAAGC-3', R: 5'-CTTGAACTCCTCTGCACCCTT-3') were used to amplify the fragment containing the mis-splicing target site which was located at the connection of exon 1 and intron 1. For rescue experiments, exogenous mRNA was first synthesized by transcription *in vitro*. Briefly, the designed primers (zebrafish *hsd17b7* mRNA primer, F: 5'-CGCGGATCCATGAAGAAAGTAGTTTTGGT-3', R: 5'-CCGGAATTCTCACATTCCATTTCTTTCTT-3'; human $HSD17B7^{WT}$ mRNA primer, F: 5'-CGGGATCCATGCGAAAGGTGGTTTTGATC-3', R: 5'-GCTCTAGATTATAGGCATGAGCCACTGA-3'; human $HSD17B7^{E182*}$ mRNA primer, F: 5'-CGGGATCCATGCGAAAGGTGGTTTTGATC-3', R: 5'-GCTCTAGACTAGAGGCTGAAATTAGATT-3') were used to amplify target DNA containing the coding sequence. Then, the pCS2 vector inserted into the amplified fragment was linearized as a template for the transcription of mRNA utilizing the SP6 mMESSAGE mMACHINE Kit (Invitrogen, #AM1340). After purifying using the RNeasy Mini Kit (Qiagen, #74104), mRNA with a 70 ng/μL concentration was co-injected into one-cell stage embryos with morpholino for rescue experiments.

sgRNA/ Cas9 mRNA synthesis and injection

sgRNA was designed against the *hsd17b7* gene (ENSDARG00000088140) using the CRISPR design tool (https://www.crisprscan.org). The sgRNA specifically targeting exon 3 of *hsd17b7* (5'-GGGAATCATGCCTAATCCCA-3') was first synthesized as follows. The GenCrispr

sgRNA synthesis kit is used to generate a gRNA DNA template with a T7 promoter and synthesize gRNA upon *in-vitro* transcription (Genscript Biotech Co.Ltd., Nanjing, China). The pXT7-zCas9 plasmid was linearized using XbaI and then transcribed in vitro to generate Cas9 mRNA using the mMESSAGE mMACHINE T7 kit (Invitrogen, #AM1344). At the one-cell stage, embryos were injected with a 2-3 μL solution containing 300 ng/μL Cas9 mRNA and 150 ng/μL sgRNA. The injected embryos were then grown in an E3 medium. At 24 hpf, genomic DNA was extracted from injected embryos, and potential CRISPR-induced mutations were identified by PCR. Primers used for identification were designed around the *hsd17b7* sgRNA target sites (F: 5'-AAAAACTTATTTTATTCCAGCCCAA-3', R: 5'-TTTCCATGCAGCACTATCAAACAATT-3').

Startle Response Test

The acoustic startle reflex was performed as described previously [30, 80]. Briefly, A plastic plate attached to a mini vibrator was used to place 20 normal larvae at 5 days post-fertilization (dpf), while an infrared digital video tracking system was used to monitor their swimming behavior. The 60 Hz tone bursts with two different sound levels of 9 dB re. m s^{-2} were applied to the amplifier to drive the vibrator. The acoustic vibration stimuli lasting for 30 ms with a 180 s inter-stimulus interval were set and applied. Each sound vibration stimulus level was repeated 20 times and the locomotion behavior of the larvae with C-shape motion to this stimulus was recorded. Finally, the movement typical parameters of mean distance and peak velocity were analyzed to assess the startle response of larvae to sound vibration stimuli.

In vitro binding assay

GST and GST-HSD17B7^{WT} fusion proteins were immobilized to GSH resins were incubated with purified His-RER1 proteins overnight at 4°C and extensively washed with washing buffer (0.3% PBST). Bound proteins were separated using SDS-PAGE and visualized with Coomassie Blue staining and Western blots.

Western blots

Frozen cells were lysed in RIPA buffer (50 mM Tris-HCl, 150 mM NaCl, 1 mM EDTA, 1%

sodium deoxycholate, 1% w/v protein inhibitor (Roche, #4693132001)) for 30 min and centrifuged at 12,000 g for 15 min at 4°C. Protein concentrations were determined using a BCA protein assay kit (Thermo Fisher, #23227).

The proteins were separated on SDS-PAGE gels and subsequently transferred to a PVDF membrane (Millipore, USA). The membranes were blocked in blocking buffer (1 × TBS containing 0.5% milk and 0.5% Tween 20) for about 45 min at room temperature, then incubated overnight with primary antibodies in TBS containing 4% BSA, 1% Tween20, and 0.05% NaN_3. Next day, the PVDF membranes were incubated with the appropriate HRP-conjugated secondary goat antibodies for 2 hours at room temperature after extensive washing with a blocking buffer. The blots were detected using ECL TM Western Blotting Detection Reagents (GE, #RPN2106), and acquired images were analyzed with ImageJ software (version 1.8.0).

Co-IP, Mass spectrum, and Gene Ontology (GO) analysis

Cell lysates from Flag, Flag-HSD17B7^{WT}, and Flag-HSD17B7^{E182*} transfected cells were incubated with 30 μL of beads conjugated to anti-Flag antibodies (Smart-Lifesciences, #SA042001) respectively overnight at 4°C. The next day, Flag beads were washed with lysis buffer 3 times, then the immune complexes were eluted with 2 × SDS sample buffer and subjected to three samples for SDS-PAGE and mass spectrum analysis.

For mass spectrum, the immunoprecipitated HSD17B7^{WT} and HSD17B7^{E182*}-associated proteins were washed and dissolved in ammonium bicarbonate buffer (25 mM, pH 8.0), followed by trypsin digestion at 37°C for 16 hours. The nano-LC-MS/MS experiments were performed with LTQ-Orbitrap MS (Thermo Fisher, USA) equipped with a Nano electrospray ion source.

For Venn diagram and GO analysis, microarray analysis identified HSD17B7^{WT} and HSD17B7^{E182*}-specific associated proteins by mass spectrum (peptide ≥ 1, unique peptide ≥ 1, P value < 0.05). Cellular component GO term enrichment analysis were performed using the web-based DAVID software [81]. Ontology networks were further investigated and visualized using R (version 4.4.1).

ScRNA-seq and data processing

Zebrafish scRNA-seq data was downloaded from NCBI Gene Expression Omnibus (GSE221471) [24]. The basic procedure for single-cell integrated data analysis was carried out in the Seurat 4.0.1 platform [82]. We selected five cell populations for re-analysis based on previous reports, including neuromast hair cells (cluster 0), supporting cells (cluster 1), macula hair cell (cluster 2), cirsta hair cell 1 (cluster 3), mantle cells (cluster 4), and crista hair cell 2 (cluster 5). Gene ontology (GO) and KEGG pathway enrichment analysis were performed using the R package clusterProfiler with the marker genes identified by Seurat V4.0.1 as the input, and the results were visualized using the enrich plot method [83].

To construct single cell trajectories, Monocle 3 (version 1.0.1) was used to cluster cells and reduce the dimensionality of gene expression matrices using UMAP. Monocle 3 package documentation was downloaded from *GitHub*. Subsets of cells that lead to the hair cell lineage were chosen using the "choose_cells" function for downstream analysis. The cells were ordered in pseudotime according to their development progress using the "order_cells" function and re-clustered in Monocle 3 for pseudotime and differential expression analysis. Cell paths were predicted by the "learn_graph" function of Monocle 3. The clusters identified as mantle cells furthest from the hair cells were chosen as the ''roots'' of the trajectory. Hair cells (cluster 0), supporting cells (cluster 1), and mantle cells (cluster 2) paths were selected separately (choose_cells) to plot their marker expression along pseudotime (plot_genes_in_pseudotime).

Mouse scRNA-seq data was downloaded from previous articles (GSE71982, (GSE168901, GSE202920) [27-29]. The basic procedure for single-cell integrated data analysis and correction of batch effects were carried out in the Seurat 4.0.1 platform [82]. We selected four cell populations for re-analysis, including inner hair cells, outer hair cells, utricle hair cells and crista hair cells.

Whole-exome sequencing and Sanger sequencing analyses

Whole-exome sequencing was performed in the proband II 1. Genomic DNA samples were extracted from whole blood samples of the proband II 1 (Figure 4A).

The exomes and flanking intronic regions from whole blood DNA samples were captured by Agilent SureSelect Human All Exon Kit (Agilent Technologies, USA). The captured DNA was sequenced on Illumina HiSeq 4000 sequencing platform (Illumina, USA). Bioinformatics were aligned to NCBI build37/hg19 assembly using the BWA (version 0.7.12) software. Each sample was covered to an average sequencing depth of at least 100×. SNPs and indels were identified using GATK HaplotypeCaller software. Candidate pathogenic variants were defined as nonsense, missense, splice - site, and indel variants with allele frequencies of 0.001 or less in public variant databases dbSNP, 1000 Genomes, ESP6500, nci60, GnomAD and in disease database of COSMIC, Clinvar, OMIM, GWAS. Genotypes distributed in every 0.3 cM of genomic region were chosen for calculation of the logarithm of odds (LOD) scores using the Merlin v. 1.1.2 parametric linkage analysis package. The proband II 1 was genotyped by Sanger sequencing analyses with designed primers (F: 5'-GTACTCTGATTGGTGACGGGTGAG-3', R: 5'- GACAGTCATAGTTCATAGTTTATT-3')

Quantification and statistical analysis

GraphPad Prism 9 (version 9.4.0) supported the whole statistical analysis. All data were repeated more than three times and presented as mean ± SD. An unpaired two-tailed student's t-test was performed for two-group comparisons, while multiple comparisons were illustrated using one-way ANOVA. The p-value less than 0.05 ($p \leq 0.05$) was considered as significantly different. $p \leq 0.05$, $p \leq 0.01$, $p \leq 0.001$, and $p \leq 0.0001$ were symbolized with "*, **, ***, and ****", respectively, and "ns" represented no significance, $p > 0.05$.

Supplementary Figures

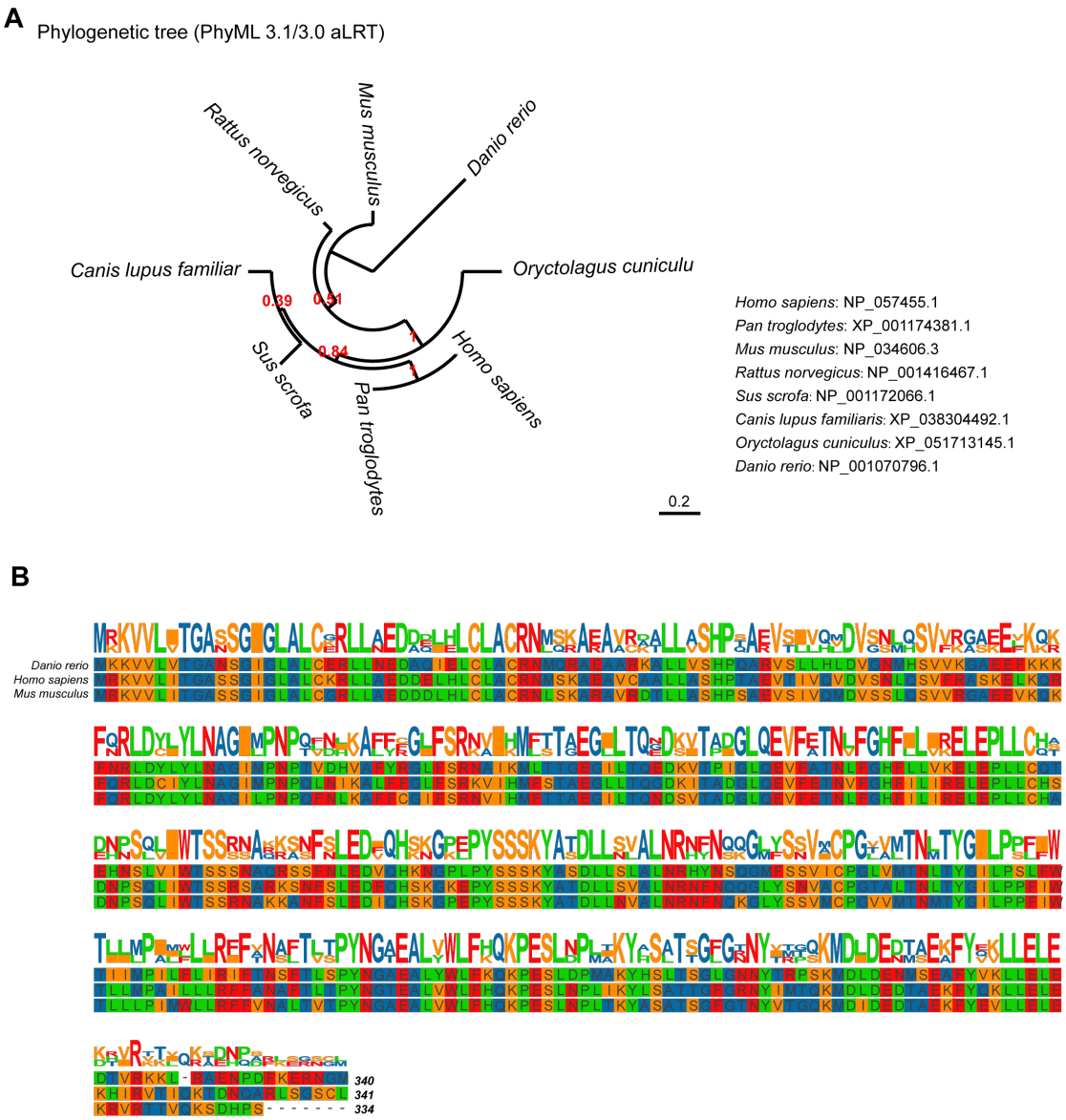

Figure S1. Evolutionary conservation of HSD17B7

(A) Evolutionary conservation of HSD17B7. The phylogenetic tree was reconstructed in the Phylogeny.fr platform (v3.1/3.0 aLRT) based on the maximum likelihood method, which graphical representation and edition were performed with TreeDyn (v198.3).

(B) The amino acid sequence was analyzed by the TBtools multiple sequence alignment of *HSD17B7* orthologs.

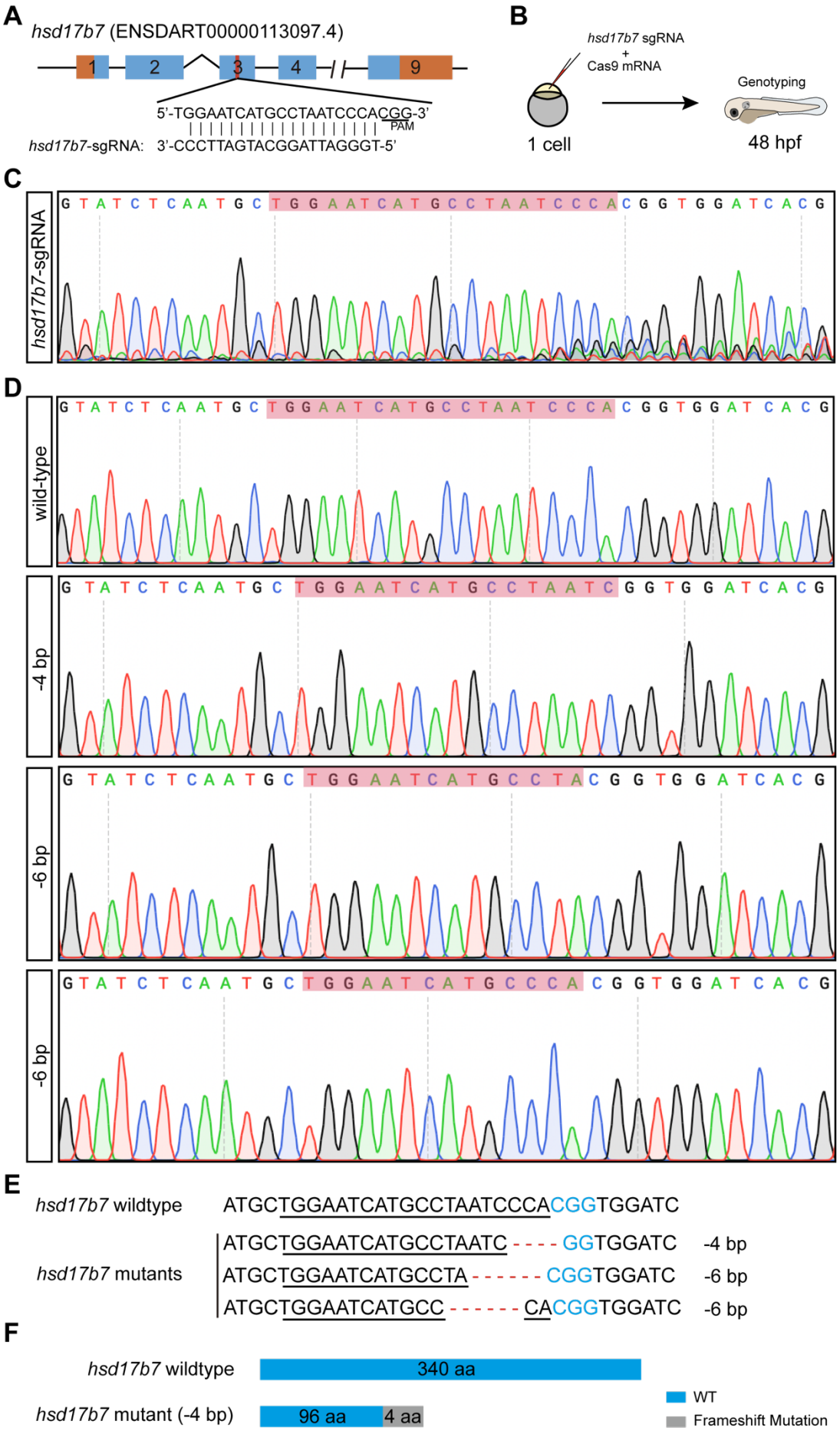
A
hsd17b7 (ENSDART00000113097.4)
1
2
3
4
9
5'-TGGAATCATGCCTAATCCCACGG-3'
PAM
hsd17b7-sgRNA: 3'-CCCTTAGTACGGATTAGGGT-5'
B
hsd17b7 sgRNA
+
Cas9 mRNA
1 cell
Genotyping
48 hpf
C
hsd17b7-sgRNA
D
wild-type
-4 bp
-6 bp
-6 bp
E
hsd17b7 wildtype
ATGCTGGAATCATGCCTAATCCCACGGTGGATC
hsd17b7 mutants
ATGCTGGAATCATGCCTAATC - - - - GGTGGATC -4 bp
ATGCTGGAATCATGCCTA - - - - - - CGGTGGATC -6 bp
ATGCTGGAATCATGCC - - - - - - CACGGTGGATC -6 bp
F
hsd17b7 wildtype
340 aa
hsd17b7 mutant (-4 bp)
96 aa
4 aa
WT
Frameshift Mutation

Figure S2. Generation of *hsd17b7* mutant using CRISPR/Cas9 system in zebrafish

(A) Schematic diagram showing sgRNA and the target site on the exon 3 of *hsd17b7* gene.

(B) Schematic diagram showing the *hsd17b7* mutant establishment process.

(C) Mutation pattern of sgRNA and Cas9-injecting embryos.

(D) Sequencing Chromatograms of -4 bp, -6 bp and -6 bp deletion mutant line

(E) Three types of mutations were identified by sequencing and screening.

(F) Schematic diagram of the predicted proteins encoded by -4 bp deletion mutant line.

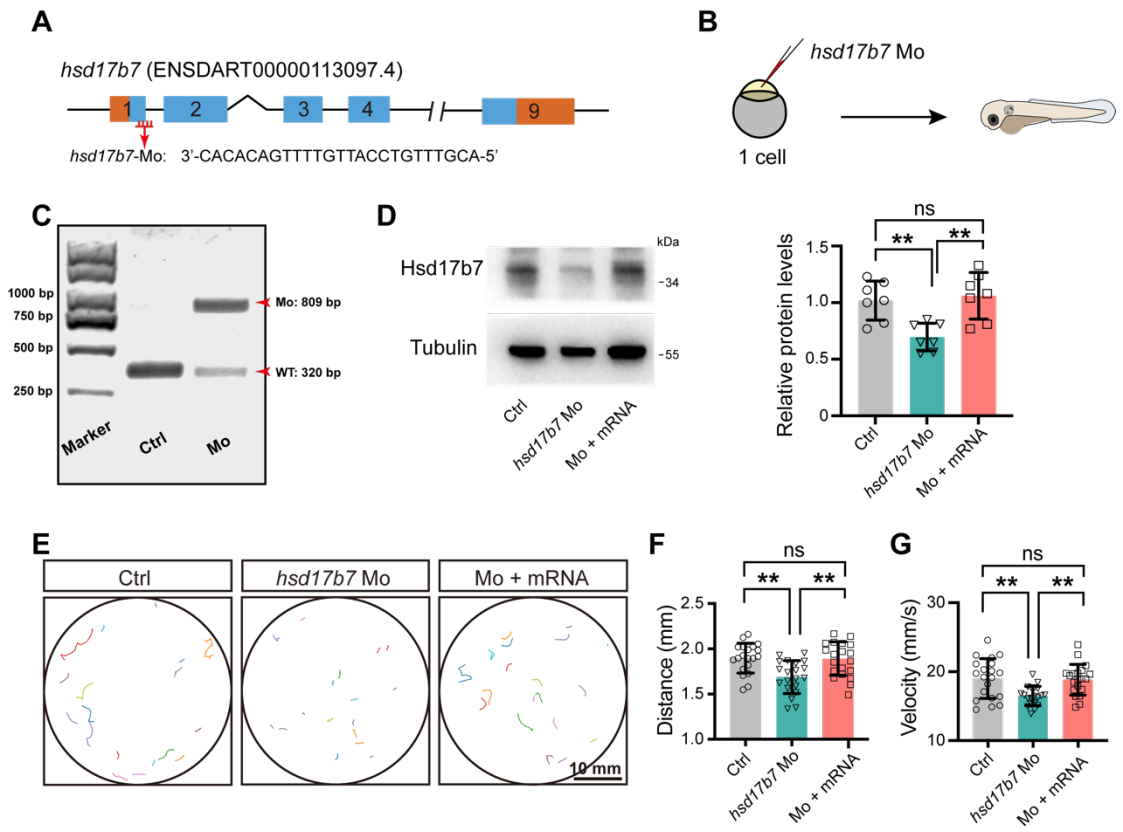

Figure S3. Knockdown of *hsd17b7* leads to auditory dysfunction in zebrafish

(A) Schematic diagram of morpholino and its target site at the exon 1/intron 1 junction of *hsd17b7* gene. (B) Schematic diagram of single-cell embryo injection of *hsd17b7* morpholino (Mo) in wild-type strain (AB). (C) The efficiency of morpholino was detected by RT-PCR. (D) Western blots showing Hsd17b7 protein levels of control, *hsd17b7* morphants, and *hsd17b7* mRNA rescued groups in whole zebrafish (3 dpf). Quantification of relative protein levels of Hsd17b7 is shown on the right (n=7). (E) Extracted locomotion trajectories from larvae with C-shape motion under a one-time stimulus of 9 dB re.1 ms^{-2} sound level with 60 Hz tone bursts in control, *hsd17b7* morphants, and *hsd17b7* mRNA rescued groups, respectively. Scale bars, 10 mm. (F) and (G) Quantification of the mean distance and peak velocity of movement at 5 dpf larvae under sound stimuli for (E) (n=20). All quantification data (D, F, and G) are presented as the mean ± SD. P values were determined using a one-way ANOVA test followed by Tukey's multiple comparisons. **$P < 0.01$; ns, non-significant, $p > 0.05$.

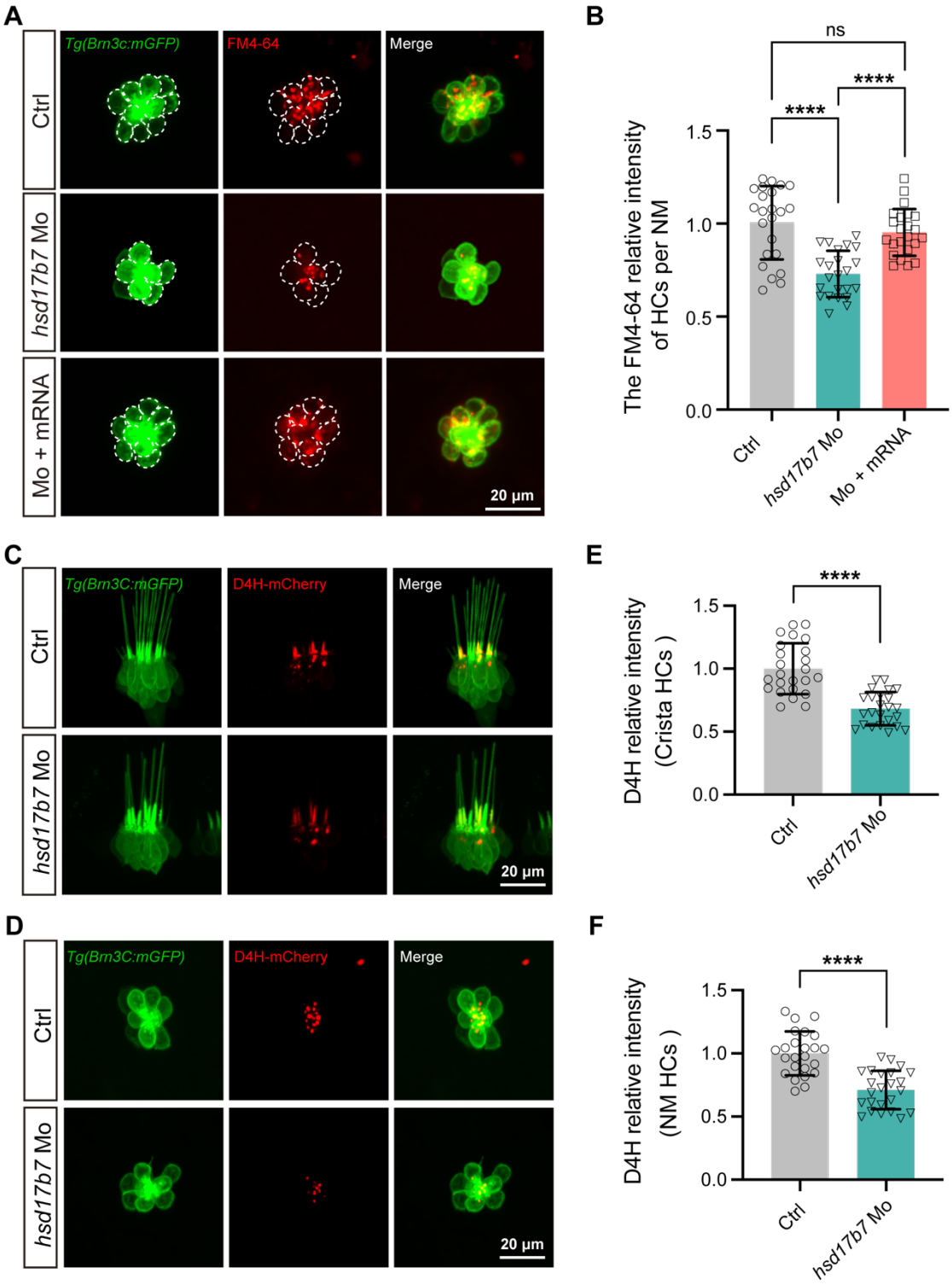

Figure S4. Knockdown of *hsd17b7* leads to MET dysfunction and decreases cholesterol levels in zebrafish

(A) Representative images of neuromast HCs (green) and functional HCs (red) in single neuromast of *Tg(Brn3C: mGFP)* at 5 dpf larvae from control, *hsd17b7* morphants, and *hsd17b7*

mRNA rescued groups, respectively. White dashed indicated neuromast HCs. Scale bars, 20 μm.

(B) Quantification of the FM4-64 relative intensity of HCs per neuromast for (A) (n=23).

(C) and (D) Representative images of cholesterol probe D4H-mCherry (red) expression in crista HCs (green) and neuromast HCs (green) of control or *hsd17b7* morphants at 4 dpf. Scale bars, 20 μm.

(E) and (F) Quantification of D4H relative intensity in crista HCs and neuromast HCs for (C, and D) (n=24).

Quantification data (B) are presented as the mean ± SD. P values were determined using a one-way ANOVA test followed by Tukey's multiple comparisons. ****$P < 0.0001$; ns, non-significant, $p > 0.05$.

Quantification data (E, and F) are presented as the mean ± SD. P values were determined using a two-tailed unpaired Student's t-test. ****$P < 0.0001$.

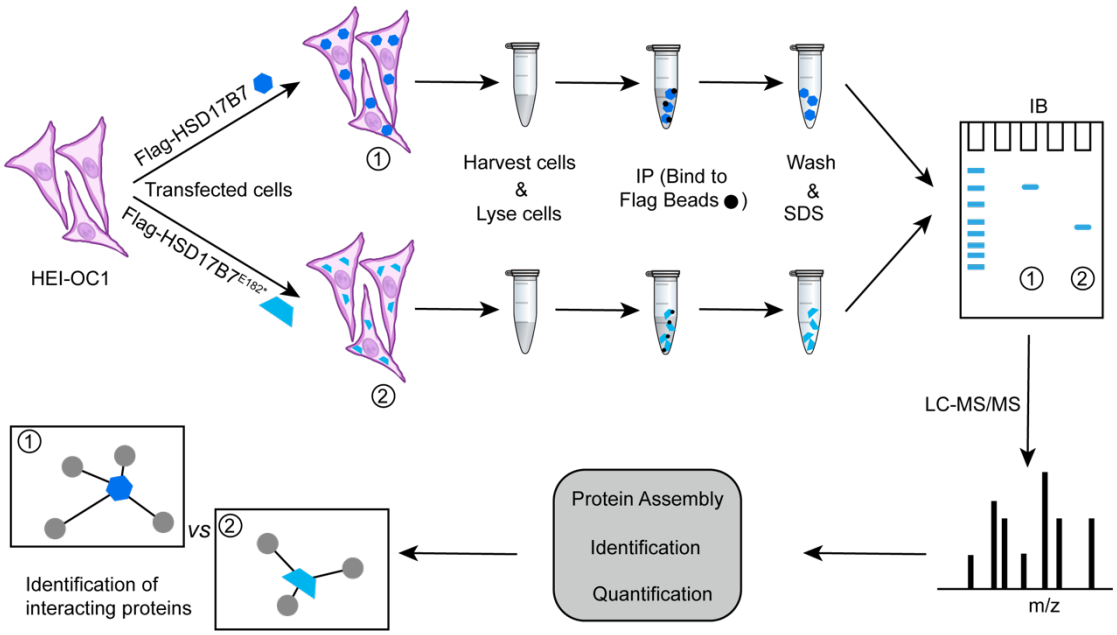

Figure S5. Schematic of the experimental process for immunoprecipitation and LC-MS/MS to identify HSD17B7^{WT} and HSD17B7^{E182*} interacted proteins.

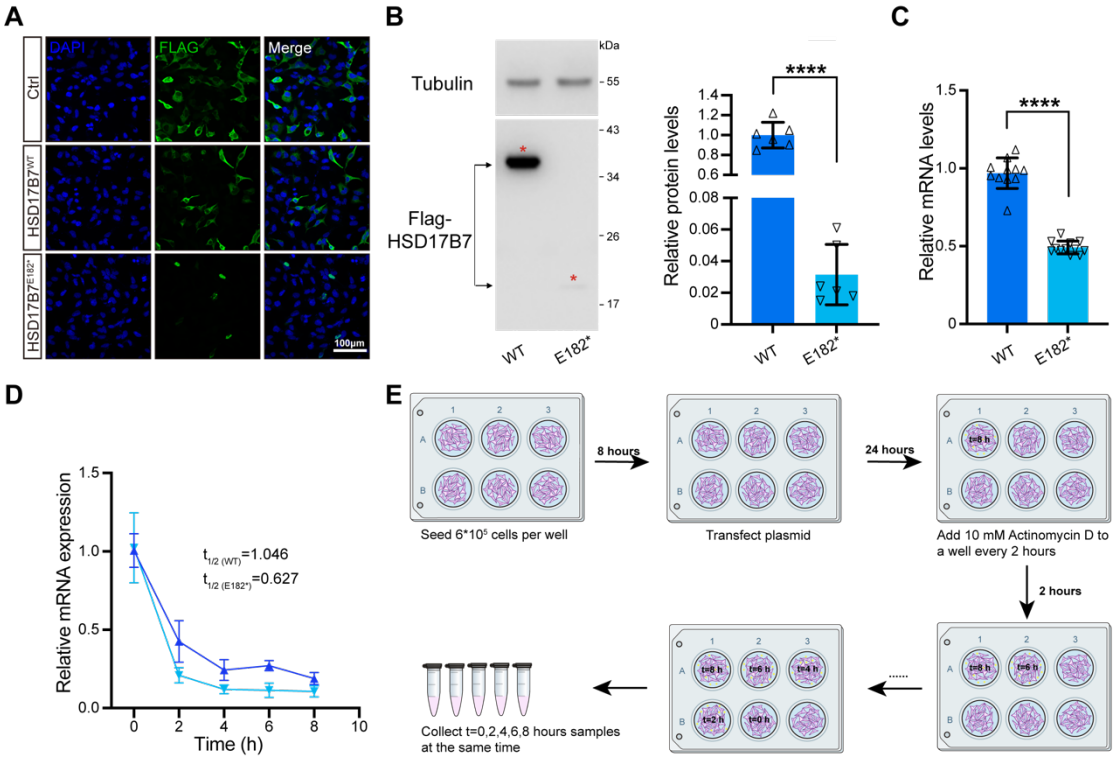

Figure S6. E182* mutation decreased HSD17B7 protein levels, mRNA levels and the half-life periods

(A) The phenomena of transfecting with pCMV2-Flag, pCMV2-Flag-HSD17B7^{WT}, and pCMV2-Flag-HSD17B7^{E182*} plasmids in HEI-OC1 cells.

(B) Western blots showing the protein levels of exogenously expressed HSD17B7 in HEI-OC1 cells transfected with pCMV2-Flag-HSD17B7^{WT}, and pCMV2-Flag-HSD17B7^{E182*} plasmids, respectively. Tubulin was used as the loading control. Red stars indicated HSD17B7^{WT} and HSD17B7^{E182*}. Quantification of relative protein levels of HSD17B7^{WT} and HSD17B7^{E182*}are shown on the right (n=6).

(C) RT-qPCR showing the mRNA level of *HSD17B7*^{WT} and *HSD17B7*^{E182*} in transfected HEI-OC1 cells (n=11).

(D) The stability of mRNA was detected by RT-qPCR in transfected HEI-OC1 cells.

(E) Schematic of the process for mRNA stability detection's experimental setup and sample collection.

All quantification data (B, and C) are presented as the mean ± SD. P values were determined using a two-tailed unpaired Student's t-test. ****P < 0.0001.

References

1. Hu, X.Y., et al., *[Prevalence of hearing disorders in China: a population-based survey in four provinces of China].* Zhonghua Er Bi Yan Hou Tou Jing Wai Ke Za Zhi, 2016. **51**(11): p. 819-825.
2. Ingham, N.J., et al., *Mouse screen reveals multiple new genes underlying mouse and human hearing loss.* PLoS Biol, 2019. **17**(4): p. e3000194.
3. Pfrieger, F.W. and N. Ungerer, *Cholesterol metabolism in neurons and astrocytes.* Prog Lipid Res, 2011. **50**(4): p. 357-71.
4. Yoon, J.H., et al., *Brain lipidomics: From functional landscape to clinical significance.* Sci Adv, 2022. **8**(37): p. eadc9317.
5. Dietschy, J.M. and S.D. Turley, *Cholesterol metabolism in the brain.* Curr Opin Lipidol, 2001. **12**(2): p. 105-12.
6. Wu, J., et al., *Impact of cholesterol homeostasis within cochlear cells on auditory development and hearing loss.* Front Cell Neurosci, 2023. **17**: p. 1308028.
7. Ding, D., et al., *Hydroxypropyl-β-cyclodextrin causes massive damage to the developing auditory and vestibular system.* Hear Res, 2020. **396**: p. 108073.
8. Levic, S. and E.N. Yamoah, *Plasticity in membrane cholesterol contributes toward electrical maturation of hearing.* J Biol Chem, 2011. **286**(7): p. 5768-73.
9. Wang, H., et al., *Deletion of OSBPL2 in auditory cells increases cholesterol biosynthesis and drives reactive oxygen species production by inhibiting AMPK activity.* Cell Death Dis, 2019. **10**(9): p. 627.
10. Yao, J., et al., *OSBPL2-disrupted pigs recapitulate dual features of human hearing loss and hypercholesterolaemia.* J Genet Genomics, 2019. **46**(8): p. 379-387.
11. Xing, G., et al., *Identification of OSBPL2 as a novel candidate gene for progressive nonsyndromic hearing loss by whole-exome sequencing.* Genet Med, 2015. **17**(3): p. 210-8.
12. Maas, R.R., et al., *Progressive deafness-dystonia due to SERAC1 mutations: A study of 67 cases.* Ann Neurol, 2017. **82**(6): p. 1004-1015.
13. King, K.A., et al., *Hearing loss is an early consequence of Npc1 gene deletion in the mouse model of Niemann-Pick disease, type C.* J Assoc Res Otolaryngol, 2014. **15**(4): p. 529-41.
14. Wang, Q., et al., *Systematic Transcriptome Analysis of Noise-Induced Hearing Loss Pathogenesis Suggests Inflammatory Activities and Multiple Susceptible Molecules and Pathways.* Front Genet, 2020. **11**: p. 968.
15. Sai, N., et al., *Involvement of Cholesterol Metabolic Pathways in Recovery from Noise-Induced Hearing Loss.* Neural Plast, 2020.

2020: p. 6235948.
16. Milon, B., et al., *A cell-type-specific atlas of the inner ear transcriptional response to acoustic trauma.* Cell Rep, 2021. **36**(13): p. 109758.
17. Zhou, Y., et al., *The susceptibility of cochlear outer hair cells to cyclodextrin is not related to their electromotile activity.* Acta Neuropathol Commun, 2018. **6**(1): p. 98.
18. Ory, D.S., et al., *Intrathecal 2-hydroxypropyl-β-cyclodextrin decreases neurological disease progression in Niemann-Pick disease, type C1: a non-randomised, open-label, phase 1-2 trial.* Lancet, 2017. **390**(10104): p. 1758-1768.
19. Tang, T.H., et al., *Can Nutritional Intervention for Obesity and Comorbidities Slow Down Age-Related Hearing Impairment?* Nutrients, 2019. **11**(7).
20. Honkura, Y., et al., *Effects of enriched endogenous omega-3 fatty acids on age-related hearing loss in mice.* BMC Res Notes, 2019. **12**(1): p. 768.
21. Sodero, A.O., et al., *Phytosterols reverse antiretroviral-induced hearing loss, with potential implications for cochlear aging.* PLoS Biol, 2023. **21**(8): p. e3002257.
22. Shehu, A., et al., *Prolactin receptor-associated protein/17beta-hydroxysteroid dehydrogenase type 7 gene (Hsd17b7) plays a crucial role in embryonic development and fetal survival.* Mol Endocrinol, 2008. **22**(10): p. 2268-77.
23. Marijanovic, Z., et al., *Closing the gap: identification of human 3-ketosteroid reductase, the last unknown enzyme of mammalian cholesterol biosynthesis.* Mol Endocrinol, 2003. **17**(9): p. 1715-25.
24. Qian, F., et al., *Single-cell RNA-sequencing of zebrafish hair cells reveals novel genes potentially involved in hearing loss.* Cell Mol Life Sci, 2022. **79**(7): p. 385.
25. Maeda, R., et al., *Functional Analysis of the Transmembrane and Cytoplasmic Domains of Pcdh15a in Zebrafish Hair Cells.* J Neurosci, 2017. **37**(12): p. 3231-3245.
26. Kindt, K.S., G. Finch, and T. Nicolson, *Kinocilia mediate mechanosensitivity in developing zebrafish hair cells.* Dev Cell, 2012. **23**(2): p. 329-41.
27. Burns, J.C., et al., *Single-cell RNA-Seq resolves cellular complexity in sensory organs from the neonatal inner ear.* Nat Commun, 2015. **6**: p. 8557.
28. Xu, Z., et al., *Profiling mouse cochlear cell maturation using 10× Genomics single-cell transcriptomics.* Front Cell Neurosci, 2022. **16**: p. 962106.
29. Wilkerson, B.A., et al., *Novel cell types and developmental*

lineages revealed by single-cell RNA-seq analysis of the mouse crista ampullaris. Elife, 2021. **10**.
30. Yang, Q., et al., *Behavioral methods for the functional assessment of hair cells in zebrafish.* Front Med, 2017. **11**(2): p. 178-190.
31. Xiao, T., et al., *A GFP-based genetic screen reveals mutations that disrupt the architecture of the zebrafish retinotectal projection.* Development, 2005. **132**(13): p. 2955-67.
32. Meyers, J.R., et al., *Lighting up the senses: FM1-43 loading of sensory cells through nonselective ion channels.* J Neurosci, 2003. **23**(10): p. 4054-65.
33. Lai, T.W., et al., *Cichoric Acid May Play a Role in Protecting Hair Cells from Ototoxic Drugs.* Int J Mol Sci, 2022. **23**(12).
34. Crumling, M.A., et al., *Hearing loss and hair cell death in mice given the cholesterol-chelating agent hydroxypropyl-β-cyclodextrin.* PLoS One, 2012. **7**(12): p. e53280.
35. Corwin, J.T. and M.E. Warchol, *Auditory hair cells: structure, function, development, and regeneration.* Annu Rev Neurosci, 1991. **14**: p. 301-33.
36. Gao, G., et al., *Kiaa1024L/Minar2 is essential for hearing by regulating cholesterol distribution in hair bundles.* Elife, 2022. **11**.
37. Schoop, V., et al., *Cellular cholesterol and how to find it.* Biochim Biophys Acta Mol Cell Biol Lipids, 2021. **1866**(9): p. 158989.
38. Cheng, H., et al., *GDC: Integration of Multi-Omic and Phenotypic Resources to Unravel the Genetic Pathogenesis of Hearing Loss.* Adv Sci (Weinh), 2025: p. e2408891.
39. Lev, S., *Nonvesicular lipid transfer from the endoplasmic reticulum.* Cold Spring Harb Perspect Biol, 2012. **4**(10).
40. Stevenson, J., E.Y. Huang, and J.A. Olzmann, *Endoplasmic Reticulum-Associated Degradation and Lipid Homeostasis.* Annu Rev Nutr, 2016. **36**: p. 511-42.
41. Yamasaki, A., et al., *Rer1p regulates the ER retention of immature rhodopsin and modulates its intracellular trafficking.* Sci Rep, 2014. **4**: p. 5973.
42. Kaether, C., et al., *Endoplasmic reticulum retention of the gamma-secretase complex component Pen2 by Rer1.* EMBO Rep, 2007. **8**(8): p. 743-8.
43. Duan, W.R., D.I. Linzer, and G. Gibori, *Cloning and characterization of an ovarian-specific protein that associates with the short form of the prolactin receptor.* J Biol Chem, 1996. **271**(26): p. 15602-7.
44. Nokelainen, P., et al., *Expression cloning of a novel estrogenic*

mouse 17 beta-hydroxysteroid dehydrogenase/17-ketosteroid reductase (m17HSD7), previously described as a prolactin receptor-associated protein (PRAP) in rat. Mol Endocrinol, 1998. **12**(7): p. 1048-59.
45. Törn, S., et al., *Production, purification, and functional analysis of recombinant human and mouse 17beta-hydroxysteroid dehydrogenase type 7.* Biochem Biophys Res Commun, 2003. **305**(1): p. 37-45.
46. Ohnesorg, T., et al., *Transcriptional regulation of human and murine 17beta-hydroxysteroid dehydrogenase type-7 confers its participation in cholesterol biosynthesis.* J Mol Endocrinol, 2006. **37**(1): p. 185-97.
47. Seth, G., R.S. McIvor, and W.S. Hu, *17Beta-hydroxysteroid dehydrogenase type 7 (Hsd17b7) reverts cholesterol auxotrophy in NS0 cells.* J Biotechnol, 2006. **121**(2): p. 241-52.
48. Ohnesorg, T. and J. Adamski, *Analysis of the 5' flanking regions of human and murine HSD17B7: identification of a cholesterol dependent enhancer region.* Mol Cell Endocrinol, 2006. **248**(1-2): p. 164-7.
49. Krazeisen, A., et al., *Determination of cDNA, gene structure and chromosomal localization of the novel human 17beta-hydroxysteroid dehydrogenase type 7(1).* FEBS Lett, 1999. **460**(2): p. 373-9.
50. Plourde, M., et al., *Analysis of 17beta-hydroxysteroid dehydrogenase types 5, 7, and 12 genetic sequence variants in breast cancer cases from French Canadian Families with high risk of breast and ovarian cancer.* J Steroid Biochem Mol Biol, 2009. **116**(3-5): p. 134-53.
51. Song, D., et al., *Expression of aromatase and 17beta-hydroxysteroid dehydrogenase types 1, 7 and 12 in breast cancer. An immunocytochemical study.* J Steroid Biochem Mol Biol, 2006. **101**(2-3): p. 136-44.
52. Wang, X.Q., et al., *Inhibition of 17beta-hydroxysteroid dehydrogenase type 7 modulates breast cancer protein profile and enhances apoptosis by down-regulating GRP78.* J Steroid Biochem Mol Biol, 2017. **172**: p. 188-197.
53. Wang, X., et al., *Synergistic control of sex hormones by 17β-HSD type 7: a novel target for estrogen-dependent breast cancer.* J Mol Cell Biol, 2015. **7**(6): p. 568-79.
54. Sang, X., et al., *Mutual regulations and breast cancer cell control by steroidogenic enzymes: Dual sex-hormone receptor modulation upon 17β-HSD7 inhibition.* J Steroid Biochem Mol Biol, 2019. **193**: p. 105411.
55. Maxfield, F.R. and G. van Meer, *Cholesterol, the central lipid*

of mammalian cells. Curr Opin Cell Biol, 2010. **22**(4): p. 422-9.
56. Subczynski, W.K., et al., *High Cholesterol/Low Cholesterol: Effects in Biological Membranes: A Review.* Cell Biochem Biophys, 2017. **75**(3-4): p. 369-385.
57. Takahashi, S., et al., *Susceptibility of outer hair cells to cholesterol chelator 2-hydroxypropyl-β-cyclodextrine is prestin-dependent.* Sci Rep, 2016. **6**: p. 21973.
58. Thoenes, M., et al., *OSBPL2 encodes a protein of inner and outer hair cell stereocilia and is mutated in autosomal dominant hearing loss (DFNA67).* Orphanet J Rare Dis, 2015. **10**: p. 15.
59. Zalewski, C.K., et al., *Auditory phenotype of Smith-Lemli-Opitz syndrome.* Am J Med Genet A, 2021. **185**(4): p. 1131-1141.
60. Chakraborty, S., et al., *How cholesterol stiffens unsaturated lipid membranes.* Proc Natl Acad Sci U S A, 2020. **117**(36): p. 21896-21905.
61. Powers, R.J., et al., *The local forces acting on the mechanotransduction channel in hair cell stereocilia.* Biophys J, 2014. **106**(11): p. 2519-28.
62. Powers, R.J., et al., *Stereocilia membrane deformation: implications for the gating spring and mechanotransduction channel.* Biophys J, 2012. **102**(2): p. 201-10.
63. Jeong, H., et al., *Structures of the TMC-1 complex illuminate mechanosensory transduction.* Nature, 2022. **610**(7933): p. 796-803.
64. Clark, S., et al., *The structure of the Caenorhabditis elegans TMC-2 complex suggests roles of lipid-mediated subunit contacts in mechanosensory transduction.* Proc Natl Acad Sci U S A, 2024. **121**(8): p. e2314096121.
65. Zhao, Y., et al., *A novel DFNA36 mutation in TMC1 orthologous to the Beethoven (Bth) mouse associated with autosomal dominant hearing loss in a Chinese family.* PLoS One, 2014. **9**(5): p. e97064.
66. Hildebrand, M.S., et al., *DFNA8/12 caused by TECTA mutations is the most identified subtype of nonsyndromic autosomal dominant hearing loss.* Hum Mutat, 2011. **32**(7): p. 825-34.
67. Vahava, O., et al., *Mutation in transcription factor POU4F3 associated with inherited progressive hearing loss in humans.* Science, 1998. **279**(5358): p. 1950-4.
68. Guan, J., et al., *Recurrent de novo WFS1 pathogenic variants in Chinese sporadic patients with nonsyndromic sensorineural hearing loss.* Mol Genet Genomic Med, 2020. **8**(8): p. e1367.
69. Zhao, J., et al., *Mutation analysis of the WFS1 gene in a Chinese family with autosomal-dominant non-syndrome deafness.* Sci Rep, 2022. **12**(1): p. 22180.
70. Tian, T., et al., *Identification of a novel MYO6 mutation*

associated with autosomal dominant non-syndromic hearing loss in a Chinese family by whole-exome sequencing. Genes Genet Syst, 2018. **93**(5): p. 171-179.
71. Li, Q., et al., *A novel KCNQ4 gene variant (c.857A>G; p.Tyr286Cys) in an extended family with non-syndromic deafness 2A.* Mol Med Rep, 2021. **23**(6).
72. Mi, Y., et al., *Early truncation of the N-terminal variable region of EYA4 gene causes dominant hearing loss without cardiac phenotype.* Mol Genet Genomic Med, 2021. **9**(1): p. e1569.
73. Kubisch, C., et al., *KCNQ4, a novel potassium channel expressed in sensory outer hair cells, is mutated in dominant deafness.* Cell, 1999. **96**(3): p. 437-46.
74. Mencía, A., et al., *A novel KCNQ4 pore-region mutation (p.G296S) causes deafness by impairing cell-surface channel expression.* Hum Genet, 2008. **123**(1): p. 41-53.
75. Zhang, J., S.S. Scherer, and S.W. Yum, *Dominant Cx26 mutants associated with hearing loss have dominant-negative effects on wild type Cx26.* Mol Cell Neurosci, 2011. **47**(2): p. 71-8.
76. Morell, R.J., et al., *A new locus for late-onset, progressive, hereditary hearing loss DFNA20 maps to 17q25.* Genomics, 2000. **63**(1): p. 1-6.
77. Wei, G., et al., *Dual-Specificity Phosphatase 14 Regulates Zebrafish Hair Cell Formation Through Activation of p38 Signaling Pathway.* Front Cell Neurosci, 2022. **16**: p. 840143.
78. Kimmel, C.B., et al., *Stages of embryonic development of the zebrafish.* Dev Dyn, 1995. **203**(3): p. 253-310.
79. Ratnadiwakara, M. and M.L. Anko, *mRNA Stability Assay Using transcription inhibition by Actinomycin D in Mouse Pluripotent Stem Cells.* Bio Protoc, 2018. **8**(21): p. e3072.
80. Gong, J., et al., *Claudin h Is Essential for Hair Cell Morphogenesis and Auditory Function in Zebrafish.* Front Cell Dev Biol, 2021. **9**: p. 663995.
81. Huang da, W., B.T. Sherman, and R.A. Lempicki, *Systematic and integrative analysis of large gene lists using DAVID bioinformatics resources.* Nat Protoc, 2009. **4**(1): p. 44-57.
82. Stuart, T., et al., *Comprehensive Integration of Single-Cell Data.* Cell, 2019. **177**(7): p. 1888-1902.e21.
83. Yu, G., et al., *clusterProfiler: an R package for comparing biological themes among gene clusters.* OMICS, 2012. **16**(5): p. 284-7.